

Target Detection and Segmentation in Circular-Scan Synthetic-Aperture-Sonar Images using Semi-Supervised Convolutional Encoder-Decoders

Isaac J. Sledge, *Member, IEEE*, Matthew S. Emigh, *Member, IEEE*,
 Jonathan L. King, *Member, IEEE*, Denton L. Woods, *Member, IEEE*,
 J. Tory Cobb, *Senior Member, IEEE*, and José C. Príncipe, *Life Fellow, IEEE*

Abstract—We propose a saliency-based, multi-target detection and segmentation framework for multi-aspect, semi-coherent imagery formed from circular-scan, synthetic-aperture sonar (CSAS). Our framework relies on a multi-branch, convolutional encoder-decoder network (MB-CEDN). The encoder portion extracts features from one or more CSAS images of the targets. These features are then split off and fed into multiple decoders that perform pixel-level classification on the extracted features to roughly mask the target in an unsupervised-trained manner and detect foreground and background pixels in a supervised-trained manner. Each of these target-detection estimates provide different perspectives as to what constitute a target. These opinions are cascaded into a deep-parsing network to model contextual and spatial constraints that help isolate targets better than either solution estimate alone.

We evaluate our framework using real-world CSAS data with five broad target classes. Since we are the first to consider both CSAS target detection and segmentation, we adapt existing image and video-processing network topologies from the literature for comparative purposes. We show that our framework outperforms supervised deep networks. It greatly outperforms state-of-the-art unsupervised approaches for diverse target and seafloor types.

Index Terms—Convolutional networks, autoencoder networks, deep learning, imaging sonar, target detection, target segmentation

1. Introduction

The detection of targets via sonar is a crucial capability for mine countermeasure and unexploded ordnance remediation missions, amongst other applications. Traditional target detection approaches rely on processing side-scan synthetic aperture sonar (SSAS) data [1] collected by a platform in a strip-map search mode. That is, the targets of interest are ensonified from a linear path wherein a of pings is recorded that contains backscatter signals from the targets over a limited, discrete range of aspect angles. Such data can be converted either into high-resolution imagery with a good signal-to-noise ratio or into acoustic color plots which capture important spectral characteristics yet only have a limited view of the targets. Various machine-learning schemes can then be applied to extract potential targets.

Circular-scan, synthetic-aperture sonar (CSAS) is another means for collecting details about underwater scenes [2–5]. CSAS relies on a sonar platform that moves in an approximately circular trajectory to ensonify local regions. As a byproduct of the approximately circular platform track, acoustic-color target templates can be obtained over the full aspect range, not just a single aspect angle as in SSAS data. As well, the beamformed CSAS imagery captures projections of the target’s three-dimensional acoustic reflectivity onto a two-dimensional imaging plane with the maximum amount of aspect-related information; that is, they are multi-aspect, semi-coherent images that provide

Isaac J. Sledge is the Senior Scientist for Machine Learning with the Advanced Signal Processing and Automated Target Recognition Branch, Naval Surface Warfare Center, Panama City, FL 32407 (email: isaac.j.sledge@navy.mil). He is the director of the Machine Intelligence Defense (MIND) Lab at the Naval Sea Systems Command.

Matthew S. Emigh is a Research Engineer with the Advanced Signal Processing and Automated Target Recognition Branch, Naval Surface Warfare Center, Panama City, FL 32407 (email: matthew.emigh@navy.mil).

Jonathan L. King is an Engineer with the Applied Sensing and Processing Branch, Naval Surface Warfare Center, Panama City, FL 32407 (email: jonathan.l.king@navy.mil).

Denton L. Woods is an Engineer with the Littoral Acoustics and Target Physics Branch, Naval Surface Warfare Center, Panama City, FL 32407 (email: denton.woods@navy.mil).

J. Tory Cobb is the Senior Technologist for Mine Warfare Automation and Processing with the Advanced Signal Processing and Automated Target Recognition Branch, Naval Surface Warfare Center, Panama City, FL 32407 (email: james.cobb@navy.mil).

José C. Príncipe is the Don D. and Ruth S. Eckis Chair and Distinguished Professor with both the Department of Electrical and Computer Engineering and the Department of Biomedical Engineering, University of Florida, Gainesville, FL 32611, USA (email: principe@cnel.ufl.edu). He is the director of the Computational NeuroEngineering Laboratory (CNEL) at the University of Florida.

The work of the first and sixth authors were funded by grants N00014-15-1-2013 (Jason Stack), N00014-14-1-0542 (Marc Steinberg), and N00014-19-WX-00636 (Marc Steinberg) from the US Office of Naval Research. The first author was additionally supported by in-house laboratory independent research (ILIR) grant N00014-19-WX-00687 (Frank Crosby) from the US Office of Naval Research and a Naval Innovation in Science and Engineering (NISE) grant from NAVSEA. The second, third, and fourth authors were supported by a grant N00014-19-WX-00897 (Dan Cook) from the US Office of Naval Research. The fifth author was supported via direct funding from the Naval Sea Systems Command.

typically superior views of targets compared to SSAS. Beamformed CSAS imagery also exhibit greatly improved shape resolution over SSAS-derived imagery [6, 7]. All of these traits make CSAS data products well suited for reducing decision-making uncertainty in automated target analysis. To date, however, there has been no use of CSAS for such applications (see section 2).

Due to the success of deep, neural-based models for SSAS-based automated target recognition [8–14] and other applications [15, 16], we believe that it can prove effective for processing CSAS-based data modalities. Here, we focus on the two-part problem of specifying target bounding boxes and extracting pixel-level target contours. We consider the subsequent problem of target classification in a companion paper.

More specifically, we propose a semi-supervised, convolutional encoder-decoder framework for detecting and separating proud targets in one or more CSAS images (see section 3). To handle detecting, tracking, and segmenting multiple targets, we use a single-branch-encoding, multi-branch-decoding convolutional network which we refer to as an MB-CEDN. The encoder branch extracts contrast features from one or more CSAS images at different spatial scales. One decoder branch highlights visually salient regions in an unsupervised manner while the other leverages supervised-trained details to label foreground and background image patches. Each of these candidate segmentation solutions are then propagated into a deep-parsing network to discover which pixels should be definitively labeled as the foreground and the background. Leveraging both candidate solutions leads to more precise target contours than when using only a single branch's guess, especially when novel target types are encountered. Moreover, we permit handling multiple CSAS images since targets may lose full-aperture coverage, and hence become difficult to spot, in different images of the same general area. Propagating and utilizing target segmentations from one sonar image also typically improves solutions for other images of the same region; analogous improvements in classification rates when using multiple area-related images have been demonstrated in [17].

We empirically assess our MB-CEDN framework using real-world CSAS imagery. We illustrate that it reliably spots and isolates multiple targets within one or more CSAS images (see section 4). Since we are the first to consider the problem of CSAS target localization, we compare against deep-network-based object detectors that have been adapted to sonar target recognition. We show that our framework yields better results than these networks and provide justifications for this performance improvement. It also outperforms state-of-the-art, non-deep saliency segmentation approaches that are unsupervised.

2. Literature Review

A great amount of research has been done for SSAS-based target analysis. For the problem of target detection, approaches can be roughly divided into two categories: either supervised or unsupervised. Conventional supervised schemes utilize shallow decision-making architectures applied to manually extracted features from SSAS-produced imagery [18–23]. For example, Dura et al. [19] provided a target detection method that employs kernel-based active learning. Mukherjee et al. [21] use an unsupervised image partitioning strategy to segment the sonar imagery. Statistical quantities are extracted from each segmented region for use in a classifier that distinguishes between potential mine and non-mine-like targets. Cartmill et al. [20] applied distributed Bayesian hypothesis testing to locate and classify buried targets. Aside from us, Barthomier et al. [24] published one of the only articles on deep-network-based detectors. They considered generic convolutional networks for creating SSAS-image region proposals. To date, no supervised or semi-supervised deep-learning-based schemes have been proposed in the literature for the combined detection and segmentation of SSAS-based imagery.

For unsupervised detection in SSAS-based imagery, most authors model acoustic highlights and shadows, along with seafloor characteristics, in an attempt to separate targets [25–32]. Early efforts in this area relied on matched filters [26] and canonical correlation analysis [27]. Dura et al. [28] later showed that acoustic shadows could be extracted using Markovian segmentation, which allowed for super-ellipses to be fit to the acoustic highlights to delineate the targets. Fandos et al. [31] utilized active contour models, among other segmentation schemes, to isolate targets from the seafloor. Williams [30] developed various efficiently computable confidence measures for target and background characteristics, such as nuisance ripples and shadow details, which were fused to create a comprehensive target-strength score. Tucker and Azimi-Sadjadi [29] employed a Neyman-Pearson detector for locating targets in dual-band, high-frequency SSAS imagery. No unsupervised deep-learning-based detectors and segmentation schemes have yet been developed for SSAS-based imagery. As in the supervised case, no combined, unsupervised-learning-based schemes are also currently available.

To our knowledge, there has been no published research on CSAS-based target detection and recognition. While the aforementioned SSAS target detectors could be applied to CSAS imagery, many would be ill suited for simultaneously handling multiple aspect angles well when rendering a detection decision. We believe that deep-network architectures would be more appropriate for this task, since a multi-aspect representation of various targets can be learned in a data-driven fashion while a robust target detector is concurrently constructed. In what follows, we review state-of-the-art deep-network architectures for natural imagery that could be adapted for sonar target detection. We then contrast our network with them to illustrate its novelty.

A majority of the state-of-the-art target detectors for natural images are convolutional in nature. OverFeat [33], regions-with-CNN-features (R-CNN) networks [34], you-only-look-once (YOLO) networks [35, 36] and many other related types of networks have exhibited vastly improved performance for object localization over traditional approaches that rely on either scale-invariant features [37] or histograms of oriented gradients [38]. OverFeat applies convolutional kernels over a sliding window on an image pyramid, which is similar to the behavior of early neural-network-based detectors. R-CNN uses a region-proposal-based strategy [39] in which each proposal is scale-normalized before being classified by a convolutional network. Spatial-pyramid-pooling networks (SPPnets) [40], in contrast, use region-based detectors that are applied much more efficiently on feature maps extracted on a single image scale. More in-vogue detectors like Fast R-CNNs [41], Faster R-CNNs [42], and region-based fully convolutional networks (R-FCNs) [43] advocate using features computed from a single scale because they offer a reasonable compromise between detection speed and accuracy.

Many recent convolutional architectures have shown how to improve object detection and segmentation by incorporating novel layer types. FCNs [43, 44], for instance, sum partial scores for each object category across different scales to produce high-quality semantic segmentations. Hyper-column networks [45] rely on an analogous approach for object instance segmentation. Several other schemes like HyperNets [46], inside-outside networks (IONs) [47], and ParseNets [48], concatenate features of multiple layers before computing predictions; this has been shown to be equivalent to aggregating sets of transformed features. Single-shot, multi-box detectors (SSDs) [49] and multi-scale convolutional networks (MS-CNNs) [50] predict objects at multiple layers of the feature hierarchy without combining features. There are also architectures that exploit lateral and skip connections that associate low-level feature maps across resolutions and semantic levels, including probabilistic UNets [51] and SharpMask [52, 53]. Another skip-connection approach was used in an FCN-type architecture and combined with Laplacian pyramids to progressively refine the object segmentations [54]. Such skip connections overcome the loss in layer-wise mutual information that occurs after stacking too many layers [55, 56]; they hence facilitate performance improvements even as the network size grows.

A commonality of these approaches is that they are supervised in nature. Owing to the large number of tunable model parameters, they hence rely on copious amounts of labeled training data to perform well. There is another class of techniques, those that are semi-supervised, that can overcome a lack of data by leveraging weak label annotations. For instance, Papandreou et al. [57] proposed to dynamically separate foreground objects from the background based on an expectation-maximization-style algorithm for training deep convolutional networks. Souly, Spampinato, and Shah [58] advocated for using generative adversarial networks (GANs) to generate additional training examples from a limited set of labeled data. Wei et al. [59] developed an adversarial erasing approach to localize discriminative image regions for segmenting objects. More recently, Wei et al. [60] showed that varying dilation rates can effectively enlarge the receptive fields of convolutional kernels in deep networks; this property was exploited to transfer surrounding discriminative information to non-discriminative object regions.

Our multi-branch, convolutional encoder-decoder network (MB-CEDN) is based on the deep encoder-decoder model with skip connections used for dense image labeling problems; FCN-like architectures [43, 44] and DeconvNets [61] have a similar composition. The encoder extracts low-dimensional, discriminative image features. The decoder then produces a candidate segmentation from those features. A difference between MB-CEDNs and previous encoder-decoder networks is that features are derived at multiple spatial scales. This improves performance for targets of different sizes. Another difference is that we incorporate two branches. One of these is trained in a supervised fashion. The other is trained in an unsupervised manner to implement saliency-based target detection. Using two branches permits focusing on unique aspects of underwater scenes. Disparate opinions about what constitutes a target are produced and can often be combined in a manner that generally improves performance over a single branch alone. The way that we handle training the unsupervised network branch is also different from previous semi-supervised schemes [57–60]. Another distinction is that our networks can co-segment multiple images simultaneously. This functionality is useful when target apertures may range from partial to complete across multiple images of the same general area and hence multiple views of the targets are required to accurately isolate all of the targets in any one image. As well, we append deep-parsing-network layers to refine the segmentation masks via random-field-like structured prediction. Refinement is a beneficial step, since we utilize scant amounts of labeled sonar data for training. Deep-parsing networks are also more efficient than conventional random-field models.

3. Methodology

In what follows, we outline our MB-CEDN architecture; network layer overviews are provided in figures 3.1 and 3.2. We focus first on the encoder followed by the dual decoding branches and subsequent post-processing using deep-parsing networks (see section 3.1). For each of these network components, we justify our design decisions. We then describe how we train the network (see section 3.2).

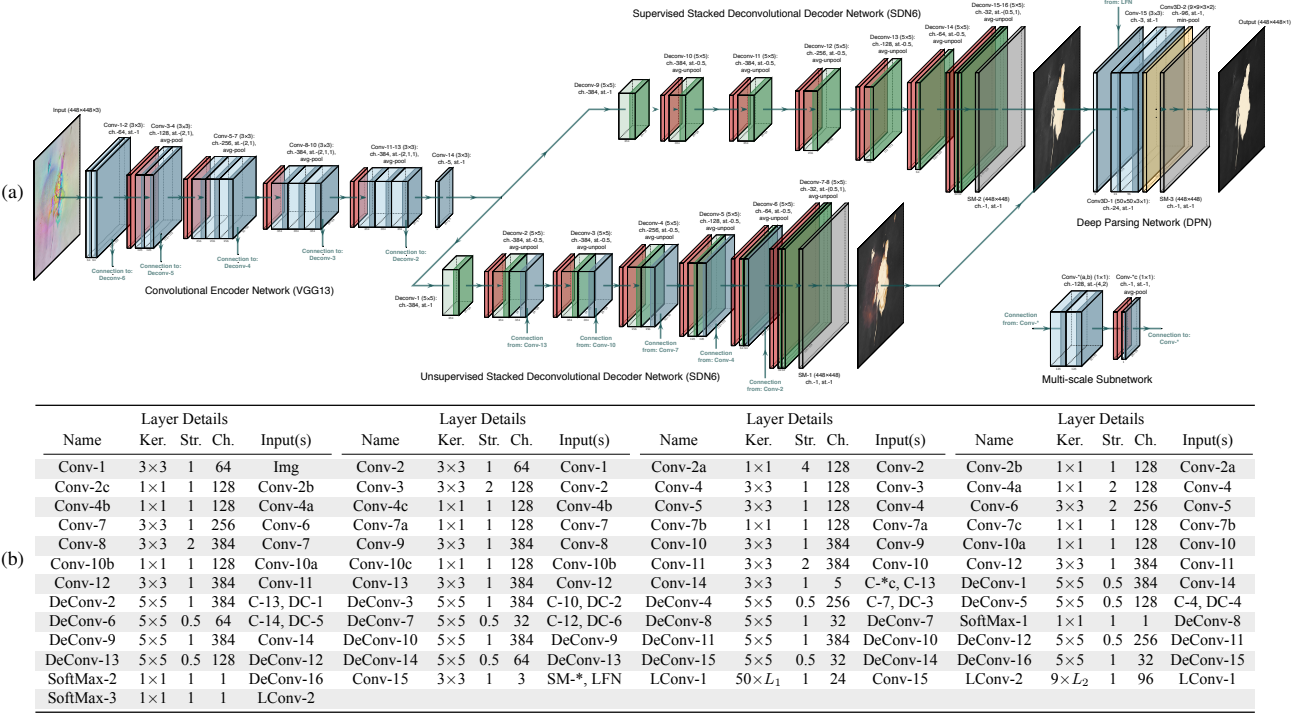


Figure 3.1: (a) A network diagram of an MB-CEDN and the resulting segmentation outputs for a CSAS image containing a crashed jet aircraft. The encoder branch of our network relies on a thirteen-layer visual-graphics-group-like network (VGG13) with residual skip connections to extract useful segmentation features. The encoder is pre-trained in a supervised fashion on natural imagery before being fit to beamformed sonar imagery. The decoder branches of our network are composed of six-layer stacked deconvolutional decoder networks (SDN6s). The unsupervised branch focuses on detecting signatures in the imagery that differ substantially from their surroundings. We use skip connections from VGG13 to refine the segmentation estimate. The remaining branch is trained in a supervised fashion to recognize target-like image regions. The responses of both branches are then combined to resolve the differing opinions as to what constitutes a potential target. When dealing with multiple images, the responses of both decoders are combined with warped estimates of the previous-computed segmentation masks. The warping is determined via processing the output of a pre-trained LiteFlowNet (LFN). Both decoder branches on a deep-parsing network (DPN) at the end to perform random-field-based structured prediction, which enhances the solution consistency. For this diagram, convolutional and deconvolutional layers are denoted using, respectively, blue and green blocks. Average pooling and unpooling layers are denoted using red blocks, while minimum pooling layers are denoted using yellow blocks. Softmax aggregation layers are denoted using gray blocks. (b) A tabular summary of the major network layers. In some instances, we shorten the names of various layers. Convolutional and deconvolutional layers are shortened to C and DC respectively, while element-wise soft max layers are shortened to SM. Asterisks are used to indicate that all layers up to that point with a particular naming convention are taken as input. That is, Conv-14 takes as input Conv-2c, Conv-4c, Conv-7c, and Conv-10c along with Conv-13. Likewise, Conv-15 takes as input SoftMax-1 and SoftMax-2 along with the output of the LiteFlowNet (LFN). For both local convolutional layers, we refer readers to the corresponding discussions for the kernel receptive field sizes.

3.1. MB-CEDN Network Architecture

Inspired by the application of fully convolutional networks to pixel-level image comprehension tasks, we would like to create a single-pass, pixel-wise network for saliency-based inference of target segmentation masks via encoder-extracted features. We also want to derive target bounding boxes from transformed versions of the features.

Our use saliency within the MB-CEDNs is pertinent for both of these tasks. Often, training examples will only encompass a fraction of the possible targets that may be encountered in real-world scenarios. Utilizing saliency to uniformly highlight attention-focusing parts of a scene helps to ensure that novel target types are not ignored.

For both of these target analysis objectives, visual contrast will play a crucial role, as it affects target perception [62, 63]. We therefore have the following design considerations. First, the MB-CEDNs should be deep enough to accommodate extracting multiple types of contrast attributes from the CSAS imagery. This is because visual saliency relies on characterizing contrast for both high-level, global features and low-level, local features to locate regions that may contain targets. Moreover, the MB-CEDNs need to model contrast across several feature maps with different scales to adequately detect targets of varying sizes and in multiple images. These features should also isolate previously seen and novel target types well.

MB-CEDN Encoder. To accommodate these desires, we re-purpose and modify the thirteen-layer visual-graphics-group (VGG13) network for dense saliency map estimation in CSAS imagery. This network acts as the encoder branch of our MB-CEDN to extract contrast features like color, intensity, and orientation. The VGG13 network is composed of five convolutional blocks, the first three of which are followed by a global average pooling layer, as shown in figure 3.1. The first block contains two convolutional layers of size $224 \times 224 \times 64$, with single strides. The first layer in this block operates on $224 \times 224 \times 3$ sliding-window input patches from CSAS images. The second block

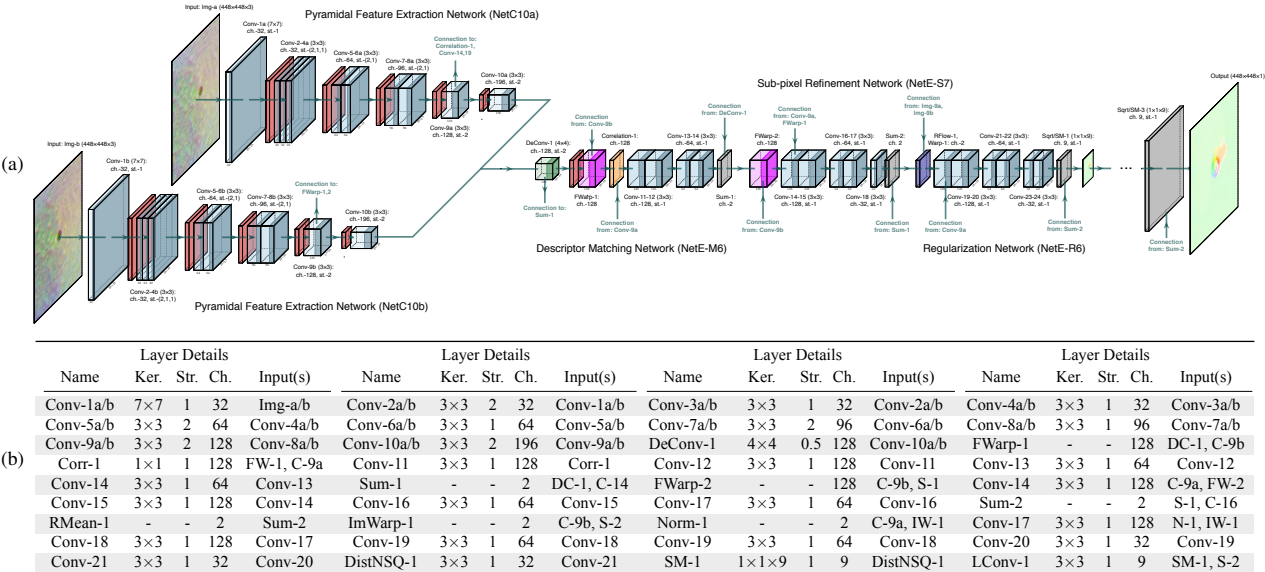


Figure 3.2: (a) A network diagram for the small-scale FlowNet model, LiteFlowNet (LFN), used to estimate the dense, large-displacement scene correspondence between two CSAS images of a clutter target. The LFN relies on dual ten-layer encoders, referred to as NetC-10s, to extract pyramidal, multi-scale features about images pairs that can be used to understand how scene content from one images changes to the next. The filter weights for both encoders are tied together. At each pyramidal level, a flow field is inferred from the high-level features. This is performed by first matching descriptors according to a NetE-M6 network. The NetE-M6 network iteratively constructs a volume of region alignment costs by aggregating short-range matching costs into a three-dimensional grid. Since the cost volume is created by measuring pixel-by-pixel correlation, the resulting optical flow estimate from the previous pyramidal level is only accurate up to that level. Sub-pixel refinement is necessary to extend the results to a new pyramidal level, which is performed by a NetE-S7 network. Lastly, to remove undesired artifacts and enhance flow vectors near target boundaries, a regularization network, referred to as NetE-R6, is used. This network relies on feature-driven local convolution to smooth the flow field in the interior of the target while preserving sharp discontinuities at the target edges. Multiple NetE-M, NetE-S7, and NetE-R6 networks are cascaded to upsample and process the flow-field estimate; these additional networks are not shown in the above diagram. For this diagram, convolutional and deconvolutional layers are denoted using, respectively, blue and green blocks. Average pooling and unpooling layers are denoted using red blocks. Softmax aggregation layers are denoted using gray blocks. Correlation layers are denoted using orange blocks. Flow warping and image warping layers are, respectively, represented by pink and dark blue blocks. (b) A tabular summary of the major network layers. In some instances, we shorten the names of various layers. Convolutional and deconvolutional layers are shortened to C and DC respectively, while element-wise softmax layers are shortened to SM. Element-wise summation layers, normalization layers, flow warping, and image warping layers are denoted by S, N, FW, and IW, respectively. Asterisks are used to indicate that all layers up to that point with a particular naming convention are taken as input.

contains two convolutional layers of size $112 \times 112 \times 128$. The remaining three blocks contain three convolutional layers each with, respectively, sizes of $56 \times 56 \times 256$, $28 \times 28 \times 384$, and $28 \times 28 \times 384$. A smaller number of channels are used, for the last two layers, than in the standard VGG13 network, since it reduces the number of tunable network parameters and improves training times without greatly impacting performance. A receptive field size of 3×3 is used for each of the convolutional filters. Leaky rectified-linear-unit activation functions are also utilized to non-linearly transform the feature maps [64], which yields good performance.

Conventional VGG13 networks only extract features at a single spatial scale. To better characterize contrast information for differently sized targets, we augment the standard architecture so that it extracts multi-scale contrast features for saliency inference. As shown in figure 3.1, we connect three additional convolution layers to each of the first four average-pooling layers. The first and second added layers use 3×3 and 1×1 convolution kernels, respectively, with 128 channels. The third added layer has a single-channel 1×1 kernel, which is used to predict the initial saliency map. To make the output feature maps of the four sets of extra convolutional layers have the same size, the stride of the first layer in these four sets are set to four, two, one, and one, respectively. Although the four produced feature maps are of the same size, they are computed using receptive fields with different sizes and hence represent contextual features at different scales. We further stack these four feature maps with the last output feature map of the convolutional network described in the preceding paragraph.

There are several additional changes that we make to the VGG13 network so that it is more suitable for target detection. The standard form of the network consists of five global pooling layers which have an increasingly smaller receptive field containing contextual information about salient targets. Each pooling layer has a stride of two, which leads to predictions that downsample by thirty-two times the input-image resolution. This can complicate saliency-map estimation, as the MB-CEDN would have to rely on copious amounts of training data to accurate process and progressively upsample such estimates in the decoder branches. We avoid this issue by increasing the prediction resolution. This is done via forcing the final two average pooling layers to have a single stride, which prevents additional downsampling, and leads to a more modest eight times reduction of the input-imagery resolution. Additionally, to maintain the same receptive-field size in the remaining layers, we apply an à-trous dilation operation [65] to the corre-

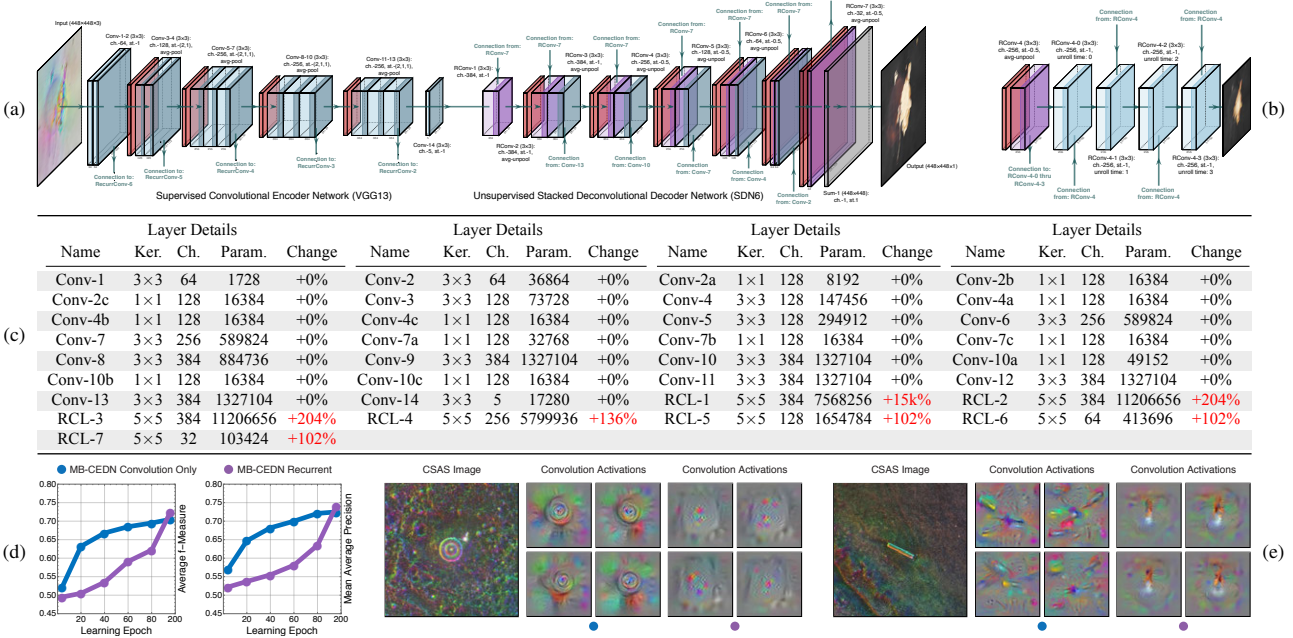


Figure 3.3: Illustrations of the disadvantages to using recurrent-convolutional layers in the upsampling process of the saliency map. In (a), we show a network diagram of a recurrent-convolutional version of the MB-CEDN for the encoder and, for simplicity, just the unsupervised decoder branch. For this diagram, convolutional and recurrent convolutional layers are denoted using, respectively, blue and purple blocks. Average pooling and unpooling layers are denoted using red blocks. Softmax aggregation layers are denoted using gray blocks. Here, each of the deconvolutional layers has been replaced with recurrent-convolution layers that are temporally unrolled for three time steps. The unrolling process introduces additional convolutional layers, one for each time step, as shown in (b). The diagram in (b) also shows that the use of recurrent-convolutional layers (RCLs) allows multiple pathways for features to propagate. This should, provided enough training samples, offer better upsampling and refinement of the encoder-extracted features than non-temporal implementations. However, the tabular summary of the recurrent MB-CEDN in (c) indicates that many times more parameters (45,074,048) need to be learned for this unsupervised encoder-decoder network compared to the purely convolutional MB-CEDN (18,074,240), which significantly hampers training. The learning statistics plots in (d) quantitatively demonstrate this behavior. Here, we plot the average f -measure and mean average precision, two statistics that measure the quality of the resulting segmentation maps. The outputs of these statistics is in the range of zero to one, with higher values indicating better performance. These plots show that the performance of the recurrent MB-CEDNs (purple) lags significantly behind that of the purely convolutional MB-CEDN (blue) except for after several hundred epochs for our 2007-image CSAS dataset. The activation maps in (e) highlight that the purely convolutional MB-CEDNs have a better grasp of particular target types and is hence able to segment them well. For example, on the left-hand side of (e), the purely convolutional MB-CEDNs encode well an axisymmetric notion of a tire after eighty epochs. On the right-hand side of (e), it can be seen that the purely convolutional MB-CEDNs have pose-invariant notion of linearly-shaped targets like tubes and casings after eighty epochs. By the same number of epochs, the recurrent MB-CEDNs are not adequately stimulated by such geometric patterns, as seen in their activation maps, and therefore do not isolate such regions well.

sponding filter kernels. This operation allows for efficiently controlling the resolution of convolutional feature maps without the need to learn extra parameters, thereby improving training times.

Another change we make is the pooling process. VGG13 networks typically rely on global max pooling to reduce the dimensionality of the intermediate network responses. Max pooling [66] has been shown to localize objects in weakly supervised networks, albeit only at a single point versus their full extent. Using such an operation in our MB-CEDNs would help learn features to detect and reliably classify targets but impede easily segmenting them. Average pooling encourages the network to identify the complete extent of the target [67], in contrast, which aids in segmentation. This occurs because, when computing the map mean by average pooling, the response is maximized by finding all discriminative parts of an object. Those regions with low activations are ignored and used to reduce the output dimensionality of the particular map. On the other hand, for global max pooling, low scores for all response regions, except that which is most discriminative, do not influence the resulting layer output. Discriminative regions of the target may hence be ignored in the dimensionality reduction process, thereby complicating their localization. Moreover, global max pooling has the tendency to propagate sonar speckle. Useful features about the targets can hence be inadvertently removed in the initial layers, unless the granular interference is eliminated beforehand.

MB-CEDN Decoders. Our MB-CEDN has two stacked decoder networks (SDNs) for converting the bottleneck-layer encoder features into saliency-based segmentation and detection estimates. The first of these isolates targets in a supervised-trained fashion, which aids in finding targets with feature characteristics similar to those that have been previous encountered during training. This branch uses a six-layer topology with a series of half-stride deconvolutions that have 5×5 receptive fields. We use deconvolutional layers of size $28 \times 28 \times 384$, $28 \times 28 \times 384$, $56 \times 56 \times 256$, $112 \times 112 \times 128$, and $224 \times 224 \times 32$ to successively transform the encoder contrast features. Global average unpooling layers are inserted after the first through fourth deconvolution layers to upsample the segmentation estimate so that it is eventually the same size as the input image. We avoid using recurrent deconvolution layers, unlike some authors

[68, 69], to refine the upsampled saliency maps. Such layers can be expensive to train since their temporal-sequence memory is tied to the state space size. They also did not appear to improve results greatly enough to warrant inclusion in our MB-CEDNs, which is highlighted in figure 3.3.

The second branch of the MB-CEDN is trained in an unsupervised manner to be a salient target detector. Its purpose is to highlight all visually salient regions, not just those that contain targets. This branch utilizes the same SDN6 architecture as the first branch. There is, however, one difference: never-closed skip connections [70] from the second, fourth, seventh, tenth and thirteenth convolutional layers in the VGG13 networks are added to the second through sixth layers in the SDN6. These skip connections serve a dual purpose. The first is that, when training in an unsupervised fashion, they promote reliable saliency labeling in the upsampling process. This occurs because high-resolution features from the encoder are cascaded with the upsampled layer output [53]. The successive deconvolution layers can then learn to assemble target-like region detection and segmentation estimates that are rather accurate despite the lack of manually labeled exemplars. Using skip connections in this manner also significantly shortens the overall training time due to avoiding singularities caused by model non-identifiability [71]. Such connections also routinely preempt a related vanishing gradient problem [72], which speeds up the learning process.

In each SDN6, there is a final prediction block that consists of two 3×3 deconvolution layers and a 1×1 pixel-wise sigmoid layer. The sigmoid layer yields normalized saliency outputs for each pixel that can be interpreted as segmentation probability maps. Another prediction block, with a 3×3 convolution layer, is employed to aggregate the responses from both decoder branches into a unified output in only a single pass.

Batch normalization [73] is applied to all deconvolution layers in both SDN6s. Its role is to improve the training speed and stability of the network by smoothing the optimization landscape [74]. Leaky-rectified-linear-unit activations are applied after batch normalization to introduce non-linearities into the feature transformation process [64], which, as we noted above, helps to yield good performance.

We allow the option of processing multiple CSAS images simultaneously, propagating previous target segmentations to guide the saliency map formation for a related area in which the sonar platform is operating and collecting data. We do this by first aligning the CSAS imagery via a pre-trained, small-scale version of the FlowNet architecture [75, 76], LiteFlowNet (LFN) [77], which is shown in figure 3.2. Such a network extracts pyramidal features from the CSAS imagery that are used to iteratively inform a regularized, dense correspondence map between image pairs. Previous labels are then transferred along the flow-field vectors to the new image. Structured local predictors [78] are employed to facilitate label consensus amongst multiple images by taking into account both local neighborhood appearance, relative position, and warped segmentation labels. The transferred segmentation estimates are then added to the decoder-branch aggregation layer.

MB-CEDN Segmentation Post-Processing. As we note below, the way that we train the MB-CEDNs causes the decoders to provide disparate interpretations of underwater scenes. Such interpretations need to be reconciled and converted into a single output response with high spatial consistency. There may also be regions with spurious labels, especially near the target edges, that need to be corrected. To handle these issues, we rely on a deep-parsing network [79] appended to the decoder branches. The deep-parsing network efficiently mimics random-field-based structural prediction, which forces neighboring locations in the combined segmentation map to have similar labels whenever the corresponding features do not deviate much. This is done by treating the encoder-branch responses as unary terms for an idealized random-field model. Such unary terms encode a mixture of label contexts and high-order relationships that quantify the cost of assigning a particular label to a given location. Dual voxel-convolution layers with sigmoid activation functions are appended to enforce pairwise constraints that promote probabilistic label smoothness on a local scale.

The pairwise-interaction portion of the deep-parsing network has the following composition. First, a single-stride $50 \times 50 \times 3 \times 1$ local convolution layer with 24 channels models contextual probabilistic constraints. A custom activation mapping [79] is used to implement a probabilistic labeling loss function that characterizes the cost of each voxel's predictions, the consistency of the predictions between voxels, and the prediction uncertainty as quantified by Shannon entropy; such a cost quantifies the local label contexts without the need for expensive-to-train recurrent layers. This first layer is followed by a single-stride $9 \times 9 \times 3 \times 2$ voxel convolutional layer with 96 channels. The second voxel layer learns a filter for the target and seafloor background classes to penalize the probabilistic label mappings from the first voxel layer. This is followed by a block, multi-stride minimum pooling layer to activate the contextual pattern with the smallest penalty and a soft-max summation layer to aggregate the unary and smoothness factors. Minimum pooling is warranted here, since we are interested in producing a discrete segmentation output that separates target-like regions from the seafloor.

Post-processing the target segmentations using a deep-parsing network is advantageous. It conducts conditional-random-field-like inference to approximate the mean-field response in only a single pass. Multi-pass schemes relying on recurrent layers require significantly more training to achieve robust label consensus. Far more training samples are also needed.

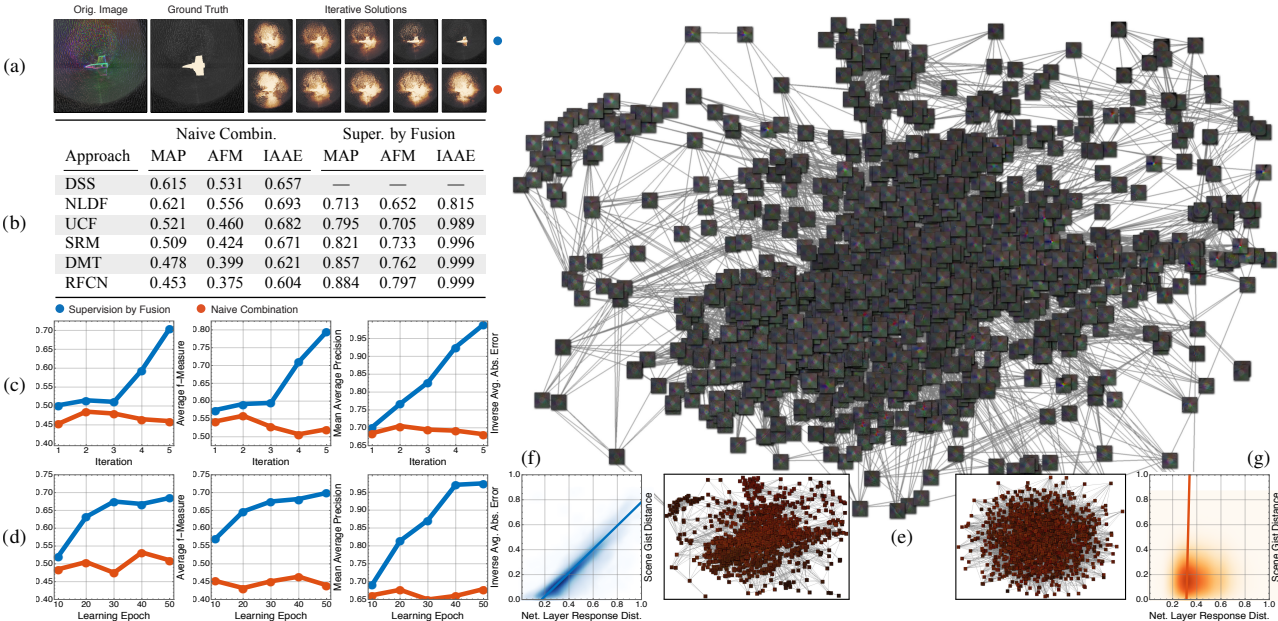


Figure 3.4: Illustrations of the disadvantages of directly training the unsupervised branch in a naive fashion. (a) A CSAS image of a crashed fighter plane and the corresponding segmentation ground truth. We show two rows of iterative learning results. The first row (blue) gives the saliency-based segmentation output for the chosen supervision-by-fusion learning approach. The second row (orange) corresponds to the results after sequentially training on a random weak detector across each iteration. In this case, the network focuses primarily on the complete-aperture region of the CSAS image, since that is the most unique aspect that is common to all detectors. (b) Statistics for this scene that indicate the achievable improvement with the addition of more weak saliency detectors. Each row corresponds to the inclusion of that detector with all previous detectors. We considered a total of six detectors: DSS [80], NLDF [81], UCF [82], SRM [83], DMT [84], and RFCN [85]. (c) Plots of the average f -measure (AFM), mean average precision (MAP), and inverse average absolute error (IAAE), for the CSAS image in (a), as a function of the learning iterations in which the pseudo ground-truth is replaced. Higher values indicate better performance. All of the statistics indicate that a naive learning approach will confuse the network, since incorrect pseudo ground-truth is propagated due to the lack of region reliability estimates. We use only three weak saliency detectors, DSS, NLDF, and UCF, for these results. (d) Statistics plots highlighting the obtainable performance across many CSAS images for the two branch training strategies when using only three weak detectors, DSS, NLDF, and UCF. (e) A t -SNE embedding of the activations for the final convolutional layer in the encoder subnetwork when trained using supervision-by-fusion; here we show the ϵ -nearest-neighbor connections in the original, non-projected space for the Euclidean distance between the activations. The original CSAS images for each projection activation are overlaid on the embedding to highlight that scenes with similar characteristics will have similar network-extracted features. We additionally superimpose polar-coordinate representations of gist features [86] for these scenes on the t -SNE embedding in (f) to show that the network self-organizes the feature representation by the visual properties of expansion, roughness, openness, and ruggedness. Supervision-by-fusion hence models well the scene segmentation difficulty, which is needed to effectively combine the weak detector results. Both the network features and gist are linearly correlated ($r^2 > 0.875$), as illustrated by the plot in (f). A naive combination strategy is unable to segment the data well, as it learns poor filter coefficients. The network activations thus have no meaningful spatial configuration in the t -SNE embedding and do not separate underwater scenes based on their visual content and difficulty, which is illustrated in (g). There is effectively no correlation with gist ($r^2 < 0.001$).

Once a consistent saliency map is achieved, layers could be appended to the MB-CEDNs to construct target bounding boxes. For our experiments, though, we instead adaptively threshold the saliency maps and use image morphology to remove any small-scale pixel regions that are likely to not contain targets. The remaining contiguous pixel regions were isolated and their maximum extents determined, which permitted fitting rectangular bounding boxes to them. This heuristic appears to yield similar performance to using more network layers, along with needing a separate training loss, to conduct bounding-box regression. However, additional labeled training samples are not required, making it advantageous.

3.2. MB-CEDN Network Training

For the MB-CEDNs to prove effective, both decoder branches should transform the encoder-derived contrast features in a way that provides complementary interpretations of the underwater scenes that are then combined into a unified response. We describe, in what follows, how this functionality can be realized by using a split training strategy with dual cost functions.

MB-CEDN Supervised Training. We would like to use human-annotated saliency maps to infer parameters for the encoder branch so that the convolutional layers extract robust, multi-scale contrast features. Likewise, we would like to use the annotated examples to train the supervised decoder branch so that targets with similar contrast characteristics as the training set are accurately detected.

Toward this end, we rely on mini-batch-based back-propagation with the following pixel-wise Shannon cross-

entropy cost function

$$\max_{\theta} \sum_{i=1}^n \sum_{j=1}^d \left(\frac{\omega_{i,j}}{n} \log(\psi_{i,j}^{\theta}) + \frac{(1-\omega_{i,j})}{n} \log(1-\psi_{i,j}^{\theta}) \right) + \lambda \|\theta\|_2^2.$$

Here, the mini-batch size is given by n , while d is the total number of pixel regions in the output saliency map. The variable λ provides the weighting for an L_2 -ridge-regularization factor, which helps prevent overfitting. The term $\omega_{i,j}$, $i=1, \dots, n$ and $j=1, \dots, d$, represents the ground-truth label at a given pixel, while $\psi_{i,j}^{\theta}$ is the predicted saliency response, from the supervised branch, at a given pixel, which depends on the network parameters θ .

The above cross-entropy cost function measures the overlap between the actual and ground-truth probabilistic saliency scores at the pixel level. Predicted saliency scores that are inconsistent with the ground-truth are penalized, leading to network parameter changes that alter the extracted local- and global-level color, intensity, and orientation features that comprise contrast. The transformation of the contrast-derived features into saliency scores, along with the upsampling and refinement processes of the corresponding saliency maps, are also adjusted so that the MB-CEDNs learn to better detect and isolate targets. An advantage to using cross-entropy is that the magnitude of the network parameter change is proportional to the saliency error. Large mini-batch errors induce major changes in the filter weights, which helps the encoder to extract progressively more meaningful features during the early learning stages when many mistakes are commonly made. Moreover, gradients do not vanish in the saturation region of the sigmoid activation function whenever the predicted and actual saliency responses become closely aligned. Adjustments to the deconvolutional filters in the supervised decoder branch can hence be made to continuously refine segmentation boundaries later in the learning process. Improved learning rates over other costs, like mean absolute error, are typically observed as a consequence of the cross-entropy-loss' behavior [87].

MB-CEDN Unsupervised Training. When using the above cost function, the supervised decoder branch will largely be effective at recognizing targets related to those in the ground-truth. It may, however, fail to detect novel targets, let alone those that are either partly buried or occluded. To help the network perform well in these instances, we want the remaining decoder branch to transform the decoder-specified contrast features in a way that highlights all salient, non-seafloor regions, not necessarily just those that are highly likely to contain targets of interest.

Furnishing sufficient human-annotated training examples to implement this salient-region detection functionality would prove challenging, though. To circumvent the need for massive amounts of labeled data, we train the second decoder branch in an unsupervised fashion using a fusion-based strategy [88]. Given n training images Ω_i , $i=1, \dots, n$, we rely on m salient target detectors [80–82] to generate pseudo ground-truth ω_k , $k=1, \dots, m$. We integrate the results from these weak detectors on both a local and a global scale, based on their estimated region-level reliability and difficulty, to provide an adequate amount of supervision for learning good filter weights. Without estimating such quantities, incorrect segmentation boundaries from one or more weak detectors will propagate through the network and significantly mislead it, as we show in figure 3.4.

From the weak saliency results, we form a series of local-image fusion maps, κ_i , $i=1, \dots, n$, that describe the local reliability of each detector for a single image. That is, for a decomposition of Ω_i into d superpixels, the regional intra-image fusion maps, $\kappa_i = \sum_{k=1}^m a_{i,k} \omega_{i,k}$, dictate how much one detector can be believed over another at labeling a superpixel as either a target or non-target. Here, $a_{i,k}$ are latent variables representing the reliability of each detector in predicting the correct saliency response for a given superpixel. Using superpixels reduces the amount of computation. They also improve spatial consistency of the saliency maps. The $a_{i,k}$ s implicitly depend on a set of difficulty variables $b_{i,j}$, $j=1, \dots, d$, which express how complicated it is for each detector to correctly label a given superpixel. Both variables are inferred using expectation-maximization for a generative model of labels, abilities and difficulties (GLAD) [89]. An overview of this fusion process, along with corresponding local and global detection results, is provided in figure 3.5.

We also combine the weak saliency results into a set of global-image fusion maps, which assess the reliability of the saliency detectors across the global scene content for all images Ω_i , $i=1, \dots, n$, simultaneously. Similar to the local-image fusion maps, the global ones, $\pi_i = \sum_{k=1}^m \alpha_k \omega_{i,k}$, rely on a set of image-level reliability variables α_k , $k=1, \dots, m$. The α_k s are inferred along with a set of image-level difficulty variables β_i using expectation-maximization within a GLAD model. Both the α_k s and β_i s depend on a set of labels that reflect the agreement of the weak saliency $\omega_{i,k}$ result with the global average saliency map $\bar{\omega}_i = \sum_{k'=1}^m \omega_{i,k'}/m$ as a function of the normalized L_1 -distance between the two maps.

For some underwater scenes, none of the weak detectors may adequately highlight potential targets, leading to poor local and global fusion maps. To preempt this occurrence, we replace the globally aggregated results that have the lowest prediction reliability with the saliency maps generated by the unsupervised decoder branch. This yields new weak saliency maps for guiding training, which, in the iteration limit, typically leads to combinations of detectors with complementary results that detect visually distinct regions well; figure 3.4 shows an example of this.

The local and global fusion maps are employed to estimate the parameters θ of the unsupervised decoder branch.

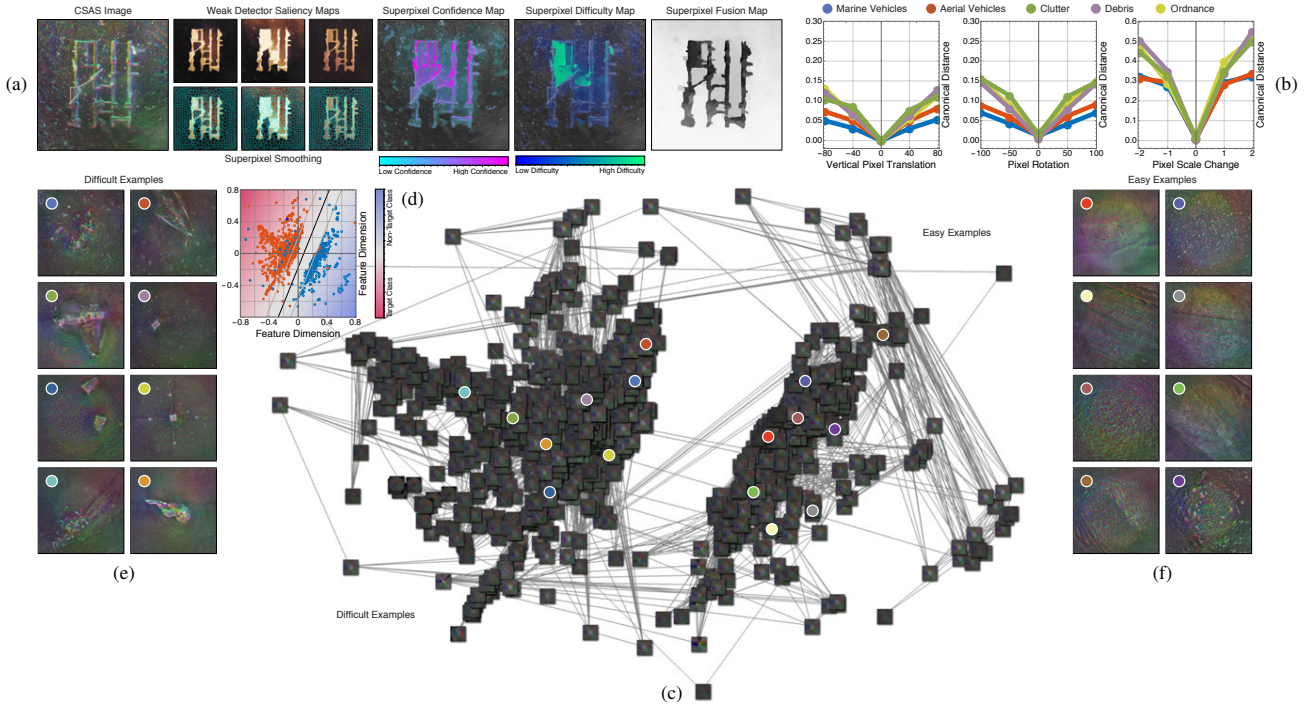


Figure 3.5: An overview of the aggregation process and its influence on detection. (a) For a given CSAS image, candidate segmentation solutions are produced using a variety of weak detectors. Warmer colors indicate a higher confidence that a given pixel belongs to a target. Superpixels are then estimated based on local scene content. The saliency scores within a superpixel region are replaced with the average saliency within that region for each map from the weak detectors. This improves the spatial consistency of the saliency-based segmentation maps by removing small-scale perturbations while preserving edge details. Local confidence and difficulty estimates are obtained for each superpixel region in each weak detection result. The aggregated confidence and difficulty estimates for the detectors are shown here. These attributes, along with the saliency scores, are integrated with a GLAD model to produce a superpixel-level saliency fusion map. A similar process is performed at the image level to obtain global fusion maps. The fused maps often better isolate targets than any weak detection result alone. (b) The resulting network contrast features that are learned through this unsupervised fusion process are rather robust. They tend to be insensitive to similitude transformations of the input images. This is corroborated by the plots of the average canonical distance between the network-extracted features, which show that the features do not change much when certain image transformations are applied. (c) A t-SNE embedding of the local and global difficulty scores for each CSAS image; here, we show the ϵ -nearest neighbor connections between underwater scenes in the original, non-projected space according to the Euclidean distance between their difficulty scores. The difficulty variables provide a near-perfect separation between scenes that contain targets and those that do not at a global image level. As shown in (d), a large-margin, linear classifier can separate scenes that contain targets and those that do not with approximately thirty errors out of over two-thousand scenes. In (e) and (f), we provide cropped CSAS images of example scenes that, respectively, contain targets and those that do not, along with color-coded indications where they exist in the projected space shown in (c). Scenes with more complexity, and hence are harder to segment, exist toward the left and right fringes of the class distributions.

This is done via mini-batch-based back-propagation with the following cost function

$$\max_{\theta} \sum_{i=1}^n \sum_{j=1}^d \frac{\gamma_i \beta_{i,j}}{n} \left(\left(\kappa_{i,j} \log(\psi_{i,j}^{\theta}) + (1 - \kappa_{i,j}) \log(1 - \psi_{i,j}^{\theta}) \right) + \left(\pi_{i,j} \log(\psi_{i,j}^{\theta}) + (1 - \pi_{i,j}) \log(1 - \psi_{i,j}^{\theta}) \right) \right) + \lambda \|\theta\|_2^2.$$

Here, the mini-batch size is given by n , while d is the total number of pixel regions in the output saliency map. The variable λ provides the weighting for an L_2 -ridge-regularization factor, which helps prevent overfitting. As well, the weight factor $\gamma_i \beta_{i,j}$, $j = 1, \dots, d$, represents the elements of the learning confidence map, which is a product of the normalized superpixel-level confidence map γ_i obtained from b_i and the normalized image-level confidence weights β_i . The terms $\kappa_{i,j}$ and $\pi_{i,j}$ indicate, respectively, elements of the local-image and global-image fusion maps, while $\psi_{i,j}^{\theta}$ is the predicted pixel-level saliency response from the unsupervised branch, which depends on θ .

For this cost function, the first scaled Shannon cross-entropy loss, penalizes the predictions which are inconsistent with the local fusion maps. The second scaled cross-entropy term penalizes predictions that are not aligned well with the global fusion maps. The interplay between both terms provides a form of complementary supervision and ensures that the predicted saliency maps will exhibit similar characteristics as the fused local and global maps. Depending on the choice of weak saliency measures, this branch can highlight targets well as a byproduct of this behavior, which we show in our experiments. As with the supervised branch, using a cross-entropy cost helps the unsupervised branch quickly adapt to major errors early during training and continuously improve from small deviations between the predicted and ground-truth saliency scores at later phases. It also handles closed-set and open-set noisy labels well [87], the latter of which naturally manifest under a supervision-by-fusion learning approach.

An additional benefit of this two-term cost function is that it leads to a blend of both self-paced-learning [90] and curriculum-learning [91] regimes. Curriculum learning guides the learning process by initially presenting the easiest

samples followed by increasingly complex ones, which yields good convergence rates and avoids poor local solutions. A sample ordering must be pre-specified, though, for it to prove effective. Self-paced learning infers such an ordering in a data-driven manner. There are, however, some differences with our cost function and conventional implementations of both self-paced and curriculum learning. First, instead of gleaning the self-paced learning weights from a learnt classifier, they are obtained from the fusion process in the form of the reliability variables. Secondly, rather than pre-defining the sample ordering and fixing it during the entire learning procedure, the ordering is updated across each iteration. Both changes lead to an adaptive style of training that further improves the convergence rate over standard curriculum learning. It also aids in uncovering visually distinct regions while ignoring many prevalent seafloor patterns, since the training process quickly switches from learning on the easy examples to those with more ambiguity and therefore leads to significant loss reductions.

MB-CEDN Joint Training. Since we rely on dual cost functions for choosing network parameters, we employ an alternating-optimization learning strategy. For each batch of training samples, we fix the weights of the unsupervised decoder branch and update the parameters of the encoder and supervised decoder branch by back-propagating the cross-entropy error. We then hold the weights for the supervised decoder branch constant and update the parameters of the encoder and unsupervised decoder using the dual cross-entropy error. In the limit, this strategy is theoretically guaranteed to converge, at least on a sub-sequence, to either saddle points or local-optimal solutions for arbitrary initial parameter guesses. This guarantee follows from the grouped-coordinate-descent theory that Zangwill [92] developed for point-to-set mappings.

4. CSAS Target Analysis Experiments

We now assess the capability of MB-CEDNs for detecting and segmenting targets in real-world CSAS imagery (see section 4.1). We demonstrate that MB-CEDNs can reliably isolate targets, regardless of their appearance and corresponding seafloor type (see section 4.2). We also show that MB-CEDNs outperform alternate saliency-based target detection approaches that have been adapted to sonar imagery from natural imagery (see section 4.2).

4.1. CSAS Experimentation Preliminaries

For our experiments, we utilize a dual-band, high-resolution, multi-element SAS sensor with an upper-end center frequency in the hundreds of kilohertz. The spatial resolution of this band is in the centimeter range. A lower-frequency band is also available, but data from it are not used in this paper.

The SAS sensor was mounted on a Hydroid REMUS 600 underwater platform; this platform operated in a variety of littoral and oceanic environments throughout the continental United States. For each of the 2007 underwater scenes, the platform maneuvered in a mostly-fixed-distance circle around one or more targets of interest, ensonifying them from all aspect angles. From the backscattered echoes, sonar images were produced and processed in a semi-coherent manner. That is, a series of coherently generated intensity images corresponding to different target looks are incoherently combined to generate a full-aperture image. Vehicle motion compensation and correction, beamforming, and image formation were performed in a manner similar to [2]. Targets were brought into focus using the automated correlation-based focusing scheme given in [3].

To improve both human interpretability and target distinguishability by our deep architecture, we color-coded the sub-apertures according to the direction of ensonification. Sub-apertures ranging from 1° to 120° , 211° to 240° , and 241° to 360° were mapped to the red, green, and blue channels, respectively.

4.2. CSAS Target Analysis Results and Discussions

4.2.1. MB-CEDN Performance

We first illustrate the target analysis behaviors of MB-CEDNs before comparing them with alternate approaches.

Training Protocols. The MB-CEDNs were trained on binary saliency maps using ADAM-based back-propagation gradient descent with mini batches [93]. An initial learning rate of 10^{-3} was chosen for ADAM. The learning rate was decreased by half every twenty epochs. We used exponential decay rates of 9.0×10^{-1} and 9.9×10^{-1} for the first- and second-order gradient moments in ADAM, respectively, which were employed to perform bias correction and adjust the per-parameter learning rates. An epsilon additive factor of 10^{-8} was employed to preempt division by zero. We used a mini-batch size of 32 samples to bias against terminating in poor local minima [94]. A ridge-regularization weight of 2.0×10^{-1} was used for both cross-entropy cost functions.

To assess detection quality, we relied on three common metrics, which were mean average precision (MAP) [69], average *f*-measure (AFM) [95], and the average intersection of the union (AIOU) [88]. For segmentation performance, we used MAP and AFM along with the inverse average absolute error (IAAE). These statistics produce values in the range of zero to one, with higher values indicating better performance.

The performance statistics that we present were averaged across 20 Monte Carlo simulations. We pre-trained the MB-CEDNs on the 23080-image PASCAL VOC 2012 dataset, with data augmentation, to implement detection behaviors and saliency-map upsampling. We then fit the them to our 2007-image CSAS dataset, again using data augmentation, to specialize to imaging-sonar characteristics. For each simulation, we randomly split and ordered the data into training, testing, and validation sets with ratios of 70%, 15%, and 15%, respectively. Pre-training on the PASCAL VOC dataset was terminated once the network loss on the validation set monotonically increased for 10 consecutive epochs. Training then commenced on the CSAS imagery and was terminated in the same fashion.

Experimental Results. Example detection results for the MB-CEDNs are provided in figures 4.1(b)(i)–(ii) and 4.1(e)(i)–(ii). For many scenes, both branches of the network detected the targets well despite the presence of various visual distractors. The supervised branch was, however, the more adept of the two at isolating previously seen targets and produced tight bounding boxes in such cases. For target types that were not witnessed during training, the unsupervised branch typically performed better. It, however, would sometimes erroneously fixated on bottom-type features, such as heavily rippled sand, rock outcroppings, and tilefish burrows, and thus led either to the addition of unnecessary bounding boxes or to boxes with an inflated size. A combination of the responses from both branches, along with processing multiple CSAS images of the same region simultaneously, resulted in the best detections, as shown in figure 4.1(g).

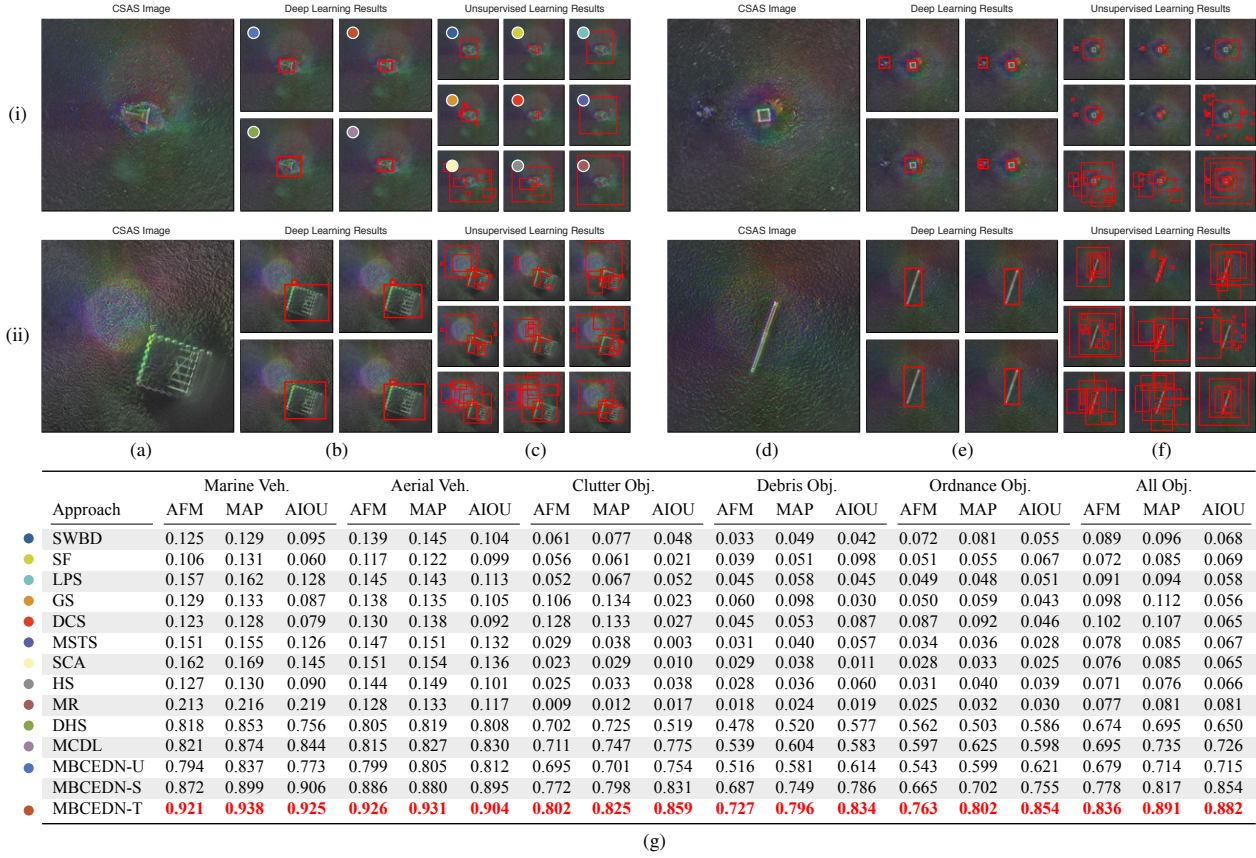
The segmentation results in figures 4.2(b)(i)–(iv) and 4.2(e)(i)–(iv) indicate that the MB-CEDN branches coherently highlight salient parts of targets well, regardless of their size or complexity. The unsupervised branch does, however, sometimes erroneously fixate on the seafloors. This primarily occurs for small-scale targets, like those in figures 4.2(b)(i)–(ii) and 4.2(e)(i)–(ii). In such cases, the amount of acoustic reflectance from the seafloor in the circular complete-aperture region is sufficiently greater compared to that in the remainder of the image; this arises from the aggregation of many acoustic pings in this region. Without either labeled examples to bias against being receptive to such acoustic interactions or more robust underlying saliency approaches used to learn the branch weights, this branch will have difficulties segregating targets from the seafloor. For larger targets, the issue was less pronounced, since the local reflectances from the targets' facets were much greater than those of the seafloor in the complete-aperture region. Despite this issue, the unsupervised branch did well for all target types, as indicated by figure 4.2(g); performance improved further if the segmentation maps were adaptively thresholded. The supervised decoder branch achieved even greater target segmentation rates due to better integrating the local and global image features. As shown in figure 4.2(g), the combination of both network branches with label consensus outperformed both.

We also note that the chosen color map helped with segmentation. Utilizing gray-scale color maps reduced average performance by anywhere from one to seven percent for all of the target classes.

Results Discussions. Our experimental results indicate that MB-CEDNs are capable of accurately detecting and segmenting targets. In what follows, we describe some of the traits that contributed to its success.

MB-CEDNs bear a strong resemblance to saliency-based, FCN-like models for target detection. MB-CEDNs are, however, able to overcome many of the FCNs' flaws, which contributed to their good performance for sonar target analysis. For instance, unlike FCNs, MB-CEDNs do not rely solely on the top-most feature map for inference. An over-reliance on top-level features may result in poor detection performance on salient regions with weak semantic information. As well, MB-CEDNs characterize features at multiple scales, which aids in accurately detecting salient targets of different sizes. This is crucial for sonar target analyses, since target dimensions can vary widely both within and between classes. FCNs detect targets at only a single scale. FCN saliency maps are also derived from fixed-size contexts, complicating the detection of target boundaries. MB-CEDNs, in contrast, have high spatial consistency, which stems from their ability to learn image-contrast features well. As hinted at by our experimental results, MB-CEDNs can infer both global contrast attributes and edge-preserving, local contrast features, both of which are combined to exclude non-salient target regions. Incorporating multiple, distinct images of the same region improves performance when one or more of these contexts are inadequate for finding low-contrast targets.

There are many other reasons why MB-CEDNs did well. In addition to learning robust, multi-scale contrast filters, MB-CEDNs adeptly removed nuisances. They did not fixate on sonar speckle, despite it being prevalent throughout the imagery. This was partly due to the use of global average pooling operations, which downsample the intermediate feature representations while generally preserving key details and removing random-phase irregularities. Complex seafloors and marine flora did little to confuse the networks. As well, the encoder convolutional kernels were tuned in a way so that the complete-aperture-region reflectances did not greatly impact the contrast features. The interaction of multiple decoding branches, each trained in a different fashion, also contributed to the overall performance. When encountering novel target types, especially those whose visual properties diverged from the target training samples, the unsupervised branch often extracted target boundaries better than the supervised branch. The MB-CEDNs weighted the unsupervised-branch responses more heavily in such cases when constructing the final saliency map. When dealing with previously encountered target types, MB-CEDNs emphasized the supervised-branch saliency maps, since they were often superior. Lastly, the use of a deep-parsing network to post-process the



(g)

Figure 4.1: CSAS target detection results. In columns (a) and (d), we provide examples of beamformed CSAS seafloor scenes for different target classes. The top scene in (a) contains a high-holding-power anchor, while the bottom scene in (a) contains an intermodal shipping container. The top scene in (d) contains a square crate and debris, while the bottom scene in (d) contains a ribbed undersea pipe segment. These scenes have been cropped near the complete-aperture region to emphasize the targets of interest. In columns (b) and (e), we provide segmentation results for four deep-learning approaches that were applied to the scenes in (a) and (d), respectively. Going left to right, top to bottom, we show the detection results for the MB-CEDN unsupervised branch (MBCEDN-U) before reaching the deep-parsing layers, the full MB-CEDN (MBCEDN-T) executed on multiple images simultaneously, where applicable, DHS [69] and MCDL [96]; we do not show the MB-CEDN supervised branch (MBCEDN-S) branch results, since they do not differ much for these examples. In columns (c) and (f), we provide detection bounding boxes for nine unsupervised saliency-based target detectors. Going left to right, top to bottom, they are: SWBD [97], SF [98], LPS [99], GS [100], DCS [101], MSTS [102], SCA [103], HS [104], and MR [105]. Note that for each target class, we detect targets in the entire scene, not just the cropped version of it shown in (a) and (d). In (g), we provide various detection statistics for the different methodologies. These include mean average precision (MAP), average f -measure (AFM) and average intersection of union (AIoU). Higher values are better and the best values are denoted using red.

saliency maps enhanced their spatial consistency. Many deep-learning-based models typically have little to no built-in means of achieving pixel-level target consensus and hence can make many more mistakes.

The way that we constructed and trained our MB-CEDNs also aided performance. For instance, a reported disadvantage of Shannon cross-entropy loss in the saliency segmentation literature is it makes pixel-wise independent predictions of the salience probabilities. The independence property can sometimes cause spatial discontinuities to form in the saliency maps, which manifest as blurry segmentation boundaries. We largely avoided this issue in our MB-CEDNs, which was a byproduct of employing deep-parsing-network layers to force the saliency scores to be spatially consistent for regions with similar contrast details. It also stems from our use of superpixels in the supervision-by-fusion training of the unsupervised branch. Super-pixels ensure that the resulting saliency score remains stable within a given cell. While some segmentation ambiguity is present, it is usually in boundary regions where targets have low-contrast content, which can occur whenever partly buried targets are encountered. Any saliency measure, without prior knowledge about these types of targets, would have difficulties in correctly labeling such regions.

Additionally, our use of fusion-based supervision permitted the generation of reliable supervisory signals from the aggregation of weak saliency models. This improved the strength of the pseudo ground-truth and led to better saliency estimates than could have been obtained by any one model. Other training strategies may not have fared as well. A naive alternative, for example, would have been to use only a single unsupervised salient target detector to provide initial pseudo-ground-truth and then training the MB-CEDN branch by using the saliency prediction results of the current iteration as supervision for the learning iteration. Only using one unsupervised salient object detector is not able to provide adequate supervision, though. Training deep models under the resulting pseudo-ground-truth maps would inevitably lead the network to build trivial feature representations and capture less informative saliency

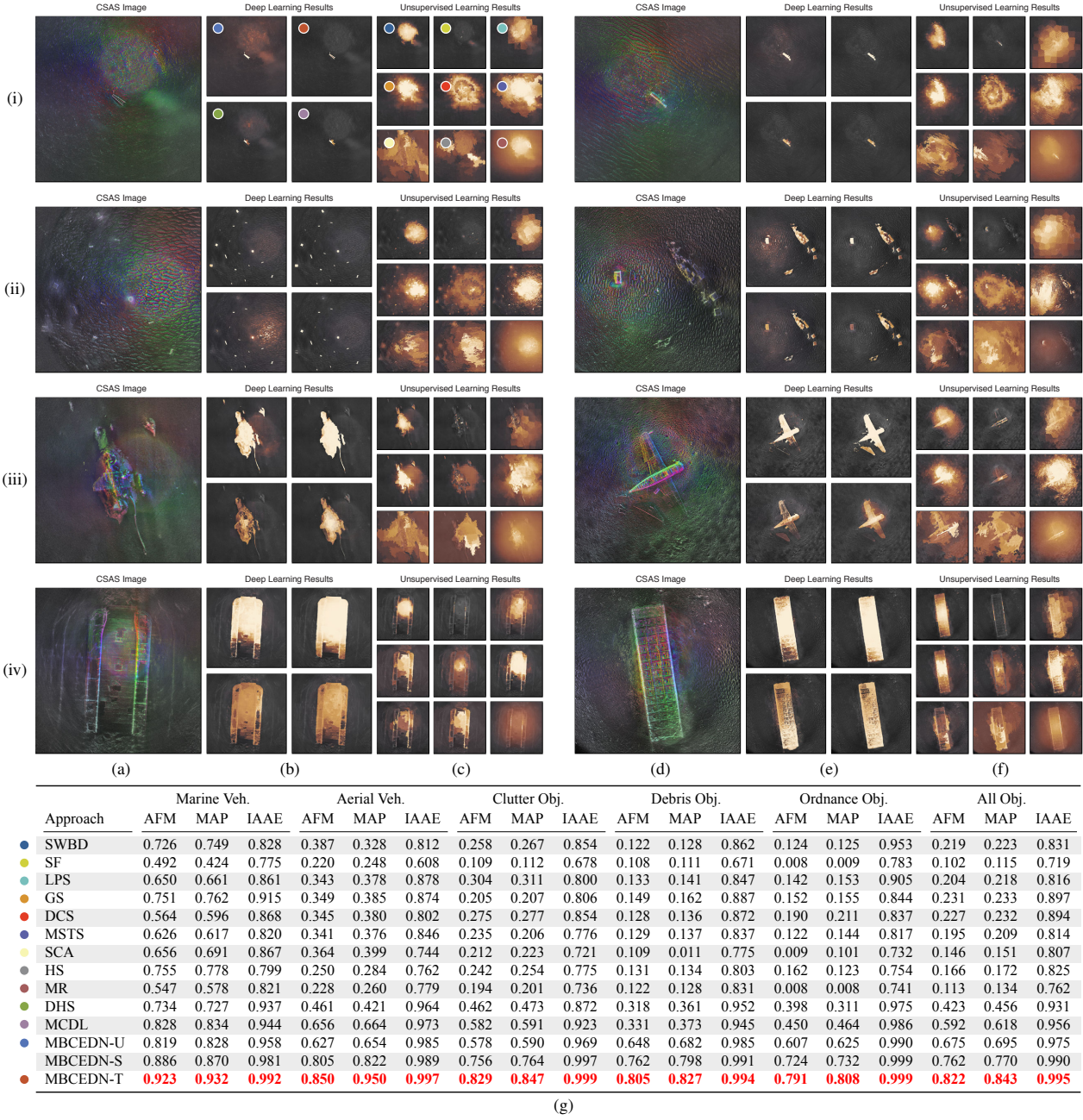


Figure 4.2: CSAS target segmentation results. Each row corresponds to results for a different target class: intact, man-made clutter, man-made debris, aerial vehicles, and marine vehicles. In columns (a) and (d), we provide examples of beamformed CSAS seafloor scenes for each class. These scenes have been cropped near the complete-aperture region to emphasize the targets of interest. Here, we have colorized the CSAS imagery based on the aspect angles associated with each sonar ping return. In columns (b) and (e), we provide segmentation results for four deep-learning approaches that were applied to the scenes in (a) and (d), respectively. Going left to right, top to bottom, we show the segmentation results for the MB-CEDN unsupervised branch (MBCEDN-U) before reaching the deep-parsing layers, the full MB-CEDN (MBCEDN-T) executed on multiple images simultaneously, where applicable, DHS [69] and MCDL [96]; we do not show the MB-CEDN supervised branch (MBCEDN-S) branch results, since they do not differ much for these examples. In columns (c) and (f), we provide detection bounding boxes for nine unsupervised saliency-based target detectors. Going left to right, top to bottom, they are: SWBD [97], SF [98], LPS [99], GS [100], DCS [101], MSTS [102], SCA [103], HS [104], and MR [105]. For the segmentation images, whiter colors denote a higher confidence that a pixel belongs to a target. More orange colors denote lower confidence scores. Note that for each target class, we segment and detect targets in the entire scene, not just the cropped version of it. In (g), we provide segmentation statistics for the different methodologies. These include mean average precision (MAP), average f -measure (AFM), and inverse average absolute error (IAAE). Higher values are better and the best values are denoted using red.

patterns. Secondly, it lacks a confidence weighting scheme, which plays an important role in guiding the network to gradually combine faithful knowledge from the confident training samples while ignoring the noisy ones. Due to the different ambiguities of the included contents, different image regions would have different difficulties for obtaining the truthful ground-truth. Treating all such training samples equally would have introduced non-negligible noise to the learning procedure and led to performance decays.

Pre-training the MB-CEDNs on natural imagery also contributed to their success. Using the PASCAL VOC

dataset stabilized the upsampling and target-detection filters in both network branches better than the CSAS dataset alone. It also was crucial for regularizing saliency in the deep-parsing-network layers. Without pre-training, the boundaries specified by the MB-CEDNs were not as well-defined as those in the presented examples. Local contexts were also often ignored, which led to difficulties in identifying the seafloor. The MB-CEDNs additionally had trouble upsampling the saliency maps.

4.2.2. Comparative Approach Performance

To provide context for the above results, we compare against deep, supervised architectures and non-deep unsupervised schemes that implement saliency-based target detection.

Training Protocols. The first supervised approach we use is deep hierarchical saliency (DHS) [69], one of the earliest, popular coarse-to-fine deep architectures for detecting and localizing targets in natural imagery. The second is multi-context deep learning (MCDL) [96], another detection network that models local and global image features to isolate targets. Both networks follow a similar encoder-decoder design and extract single-scale contrast features to form an initial segmentation solution that is iteratively refined. While there are many other available detection architectures, they typically resemble these two and, based on our prior experiments, are not likely to yield meaningful performance improvements.

Training of both schemes proceeded as follows. For MCDL, we initialized the underlying Clarifi network weights using those from the ImageNet 2013 competition. The remaining layer weights were randomly chosen. The network was trained using ADAM-based back-propagation gradient descent with mini batches and data augmentation. A unified soft-max penalty between the classification result and the ground-truth label was employed as the loss function; this loss was factorized into a product of experts, as described in [96]. The hyperparameter values were the same as those for our MB-CEDNs. We also employed the same data splitting strategy as above for the CSAS data.

For the DHS network, we initialized the encoder weights from an ImageNet-trained VGG13 network. The decoder weights were randomly selected. The entire network was then trained, end-to-end, on the PASCAL VOC 2012 dataset using momentum-based back-propagation gradient descent with mini batches and a cross-entropy loss. Similar to the authors of [69], we unfolded the recurrent-convolution layers to avoid the need for training with back-propagation-through-time. We used a mini-batch size of 12 samples. Initial learning rates of 1.5×10^{-2} and 1.5×10^{-3} were chosen for the final layer and remaining layers, respectively. The learning rate was halved after being presented with 4×10^4 samples. Momentum and decay factors of 9×10^{-1} and 5×10^{-4} were, respectively, utilized. We then fit the network to our CSAS imagery dataset. Mini-batch sizes of 5 samples were used. The initial learning rates for the last and remaining layers were lowered to 3×10^{-2} and 3×10^{-5} , respectively. For the remaining parameters, we used the same values as in our MB-CEDNs. We also used the same data splitting strategy as above.

We additional compare against nine unsupervised saliency-based target extractors. These include saliency with background detection (SWBD) [97], saliency filters (SF) [98], learning-to-promote saliency (LPS) [99], geodesic saliency (GS) [100], dictionary-CRF saliency (DCS) [101], minimal-spanning-tree saliency (MSTS) [102], saliency cellular automata (SCA) [103], hierarchical saliency (HS) [104], and manifold ranking (MR) [105]. These schemes rely on image appearance and region-connectivity details to distinguish between conspicuous target and background pixels. Many also integrate image-based priors in an attempt to improve detections in both cluttered scenes and those with low-contrast backgrounds.

For each of these approaches, we used the same saliency-thresholding and image morphology heuristic as in our MB-CEDNs to identify individual pixel regions that were likely to contain targets. The maximum extents of each region were used to define bounding boxes. Employing this heuristic allowed for a fair comparison against the MB-CEDNs, as performance was driven solely by the underlying saliency-producing processes.

Comparative Experimental Results. Detection results for DHS and MCDL are given in figures 4.1(b) and 4.1(e) for the four underwater scenes depicted in figures 4.1(a) and 4.1(d). These example scenes show that both DHS and MCDL can reliably spot targets with few spurious detections. Overall, however, both DHS and MCDL lag behind the performance of MB-CEDNs, which is apparent from the statistics presented in figure 4.1(g). There are a few reasons for this. In some scenes, DHS and MCDL completely miss small-scale targets, like spent munitions, that do not have complete aperture coverage and hence are not easily distinguished from the seafloor. The approaches are sometimes confounded by environmental artifacts, such as rock outcroppings, that appear visually similar to debris and clutter. DHS and MCDL also have a propensity to slightly over detect, in the sense that they create multiple, overlapping detection boxes instead of merging them; an example is shown figure 4.1(e)(i), where the debris is unnecessarily fragmented into many components. Additionally, both approaches do not always fit tight bounding boxes around the targets, unlike our MB-CEDNs; this can be seen in figures 4.1(b)(i) and 4.1(e)(i), where the disturbed seafloor sediment is incorrectly included with the ship anchor and container detection regions, respectively.

Sample segmentation results for the DHS and MCDL networks are provided in figures 4.2(b) and 4.2(e) for the eight underwater scenes in figures 4.2(a) and 4.2(d). Both networks segmented well when targets had complete aper-

ture coverage. They coherently highlight the man-made clutter and debris in figures 4.2(b)(i)–(ii) and 4.2(e)(i)–(ii), for instance, regardless of how small the targets became and the complexity of the seafloor. Segmentation performance quickly fell when complete aperture was lost, though. Some targets, like the man-made debris and spent munitions in figure 4.1(b)(ii) were either missed entirely or only partly captured in these cases. Larger targets suffered from the same issues. For the airplane wreckage in figure 4.2(e)(iii), parts of the sheared tail fin and wings were not completely isolated, for both DHS and MCDL, due to both low-contrast acoustic highlights and a lack of total aperture coverage. When using DHS, diagonal indentations in the wings were considered part of the seafloor, which were caused by acoustic shadows. Acoustic shadows also stymied the segmentation process for the sunken amphibious transport in figure 4.2(b)(iv) and the capsized barge in figure 4.2(e)(iv); either more training samples or post-processes, such as region-based label consensus, would be needed to correct such mistakes, as we discuss below. The statistics presented in figure 4.2(g) indicate that these types of issues contributed to worse performance compared to our MB-CEDNs.

Comparably, all of the unsupervised, saliency-based approaches yielded worse detection results than the deep, supervised networks. Figures 4.1(c)(i)–(ii) and 4.1(f)(i)–(ii) show that they produced many spurious bounding boxes which frequently either missed the targets or predominantly contained just the seafloor. Such boxes often coincided with ensonified regions where the number of available apertures was changing, which resulted in color-map pattern shifts and hence locally distinct image cues. For example, for the ship-anchor scene in figure 4.1(a)(i) and the water-outflow-structure scene in figure 4.1(a)(ii), SWBD, GS, DCS, HS, and MR, all unnecessarily fixated on the circular, complete-aperture area where the color variation is highly pronounced. The scenes in figure 4.1(d)(i)–(ii) show that this occurred even if the color-map variation was not overly conspicuous. Erroneous bounding boxes were also added due the sensitivities of LPS, DCS, MSTS, SCA, and HS to sonar speckle and acoustic reflectance from small-scale, non-target artifacts; many of these boxes are not displayed in figure 4.1(c)(i)–(ii) and 4.1(f)(i)–(ii), since they often encompassed only a few pixels and were removed via post processing. Moreover, schemes like SF and DCS typically failed to isolate the entire target, let alone large fractions of it, due to being receptive primarily to edges that arise from high-intensity acoustic returns. In figures 4.1(c)(ii) and 4.1(f)(ii), for instance, the bounding boxes traced the dominant outlines of the water-outflow structure and the ribbed pipe segment, respectively. All of these issues, and others, contributed to the lower-than-expected detection scores given in figure 4.1(g).

The segmentation plots in figures 4.2(c)(i)–(iv) and 4.2(f)(i)–(iv) offer some additional clues as to why the detection rates were poor for these unsupervised schemes. SWBD, DCS, LPS, GS, MSTS, and many related approaches can miss small-scale targets, such as discarded steel drums, artillery shells, and exposed piping, even when they are located in the complete-aperture region. This occurs because the color-map changes are pronounced in this region and hence yield a stronger local-image-cue response than the color-map variations from targets. Changing the color map did not improve performance. Different seafloor types, such as rippled sand, also disrupted the segmentation process. Additionally, the use of compactness and objectness image priors forces the unsupervised schemes to treat small-scale objects as nuisances; they hence are ignored. Size and location priors, like those used in MR, further contribute to the poor segmentation performance of small-scale targets, since they incorrectly assume that targets will be positioned toward the center of the CSAS imagery. For larger-scale targets, like the sunken amphibious transport in figure 4.2(a)(iv) and the capsized barge in figure 4.2(d)(iv), many of the unsupervised schemes fared better. The color-map variation for such targets was often much higher than that for the seafloor, which allowed the local-image cues to more reliably fixate on them. However, there were so few of these target types, compared to the other classes, which significantly impacted the overall segmentation performance, as shown in figure 4.2(g).

Results Discussions. The above results indicate that supervised saliency-based target detectors significantly outperformed their unsupervised counterparts. Moreover, none of the competing methodologies either detected or segmented as well as our MB-CEDNs. There are several reasons why this occurred, which we explain below.

Much like our architecture, DHS coarsely detects salient objects from both local and global contexts then proceeds to progressively upsample the estimated saliency map in a hierarchical manner. A key difference of DHS, though, is that saliency-map refinement is iteratively performed using multi-pass recurrent-convolutional layers versus one-pass convolutional layers in MB-CEDNs. The use of recurrent-convolutional layers permits filters in each layer to be modulated by other filters in the same layer, thereby, in theory, enhancing the capture of meaningful details about the context of the targets. This can result in upsampled saliency maps that preserve well target boundaries and remove superfluous target-detection uncertainties. In practice, however, DHS-like models require a great deal of training to adequately perceive global target properties and avoid the distraction of local interferences. This happens since the recurrent-layer memory grows exponentially as a function of the state-space size. Large swaths of the state space must hence be visited during training to characterize well the next-state dynamics and hence yield reasonably good detections. This did not occur here, due to the scant amount of available CSAS imagery. The DHS networks hence did not generalize as well as the MB-CEDNs for segmenting targets. MB-CEDNs, in comparison, relied on more efficient and accurate deep-parsing networks, which avoided the use of recurrent layers for learning conditional-

random-field-like structured predictions. The target boundaries hence remained more consistent, even when local segmentation mistakes were made during upsampling.

The MCDL network is another hierarchical model for saliency-based target detection. Akin to our architecture, MCDL characterizes saliency in a multi-context fashion. Global contexts are employed to estimate the saliency of potential targets across the entire image, while local contexts are used for localized prediction near target boundary regions and in areas where there is much textural detail. In the MCDL framework, both contexts are modeled explicitly and integrated whereas the context representations are mixed in the MB-CEDNs. Separating the context extraction should, in theory, yield better-performing detection and segmentation results. For instance, semantically salient targets should be better localized in low-contrast and cluttered backgrounds when explicitly modeling and optimally consolidating visual cues, background priors, and various high-level target details. Practically, though, MCDLs underperform MB-CEDNs due to several factors. Foremost, MCDL networks are distracted by local salient patterns in cluttered backgrounds, due to their sensitivity to sonar speckle. This stems from the use of average max pooling, versus global average pooling, in the underlying Clarifai feature-extraction networks. As well, MCDL infers saliency maps in an isolated, patch-wise manner, implying that crucial spatial information both the input image and intermediate-layer feature maps is ignored. The inclusion of fully connected layers is to blame for this issue. Fully connected layers also add several times more parameters than our MB-CEDNs, which complicates the adaptation from natural imagery to sonar imagery. Lastly, since all the image patches are treated as independent samples during network training and inference, there is no shared computation among overlapping image segments, which results in significant redundancies that do not necessarily aid in detection.

Perhaps the biggest contribution to the MB-CEDNs' success was the extraction and transformation of multi-scale color, intensity, and orientation features. This helped the networks to detect targets well, regardless of their size and orientation. Our chosen dual-cost training strategy aided this process, as it often quickly converged to good contrast filters. DHS and MCDL networks, in comparison, only characterize contrast at a single scale. They hence have difficulties in accurately isolating small-scale targets, like certain types of debris and ordnance, which can be seen from the reported segmentation statistics.

Conventional unsupervised saliency methods for target detection rely on various image cues. The most widely employed is contrast, which measures the distinctiveness of image regions with respect to either local or global contexts. Local contrast methods tend to highlight target boundaries while missing much of the interiors. Global contrast approaches often uniformly highlight target interiors, thereby leading to better-performing detectors. They still are unsatisfactory, however, as we saw in our experiments with SF, GS, LPS, HS, and other techniques. It has been previously shown that global contrast fails to preserve important target details. They often have difficulties detecting small-scale targets and those with complex textures. This issue is exacerbated when the scene backgrounds are either cluttered or have a similar appearance to the targets. Many have built-in fixation schemes, which emphasize patterns near the center of the image; such an assumption is not always appropriate for CSAS imagery, since targets may be present outside the complete-aperture region. Moreover, these schemes often evaluate contrast using hand-crafted features, like intensity, color, and edge orientation, which are chosen based on the current limited understanding of human attention. The preferred color mapping for CSAS imagery differs wildly from what is typically observed in natural imagery, which impedes many of the color-based features and yields several erroneous detections. Alternate color maps, even gray-scale ones, have issues, due to the multi-directional acoustic highlights. Hence, without the ability to adapt to sonar-image characteristics, these low-level, unsupervised approaches will likely not generalize well to underwater scenes; the poor detection statistics that we presented for SF, GS, HS, and other schemes corroborate this claim.

Some more recent salient detection approaches that we considered in our experiments incorporate prior knowledge into cues in an attempt to improve performance. Background priors used in methods like SWBD encourage regions near image boundaries to be labeled as part of the background. However, such an assumption can fail when targets either have a similar appearance with backgrounds or intersect image boundaries. Compactness priors, used by SF and other approaches, favor targets that are compact and perceptually homogeneous elements. They can fail for large-scale targets, though, like many of the scuttled marine vehicles. Objectness priors tend to highlight regions which may contain targets of a certain class. Although such priors can help isolate targets, they are typically implemented using hand-designed features with implicit assumptions. These assumptions do not always translate well from natural imagery to sonar imagery; they, for instance, fixate on spurious artifacts, like speckle. Some methods combine cues to utilize their complimentary interactions and improve overall performance in certain cases. These works, however, usually rely on shallow learning models, which make characterizing complicated joint interactions between diverse saliency cues difficult. Moreover, to preserve conspicuous target details and subtle structures, many methods adopt over-segmentations of images, like superpixels used by LPS; such representations are used either as the basic computational units to predict saliency or as the post-processing methods to smooth saliency maps. Although these methods can improve saliency detection results for large-scale targets, they may not always be relevant for smaller ones unless the superpixel size can be adapted.

5. Conclusions

We have proposed a novel deep-network architecture for saliency-based detection and segmentation of targets in CSAS imagery. Our work represents the first automated target analysis effort for such an imaging-sonar modality. It is one of only a small number of deep network approaches for target detection in any imaging-sonar modality.

Our multi-branch network, the MB-CEDN, relies on a convolutional encoder-decoder architecture. The multi-layer encoder portion of the network extracts features that permit detecting and segmenting targets coarsely from a global and local context. Dual stacked decoders with skip connections are cascaded to transform the contrast features into a segmentation map and progressively improve it by integrating local image contexts. These decoders are trained in a supervised and unsupervised fashion and, respectively, perform well when encountering previously seen and novel target types. A deep-parsing network then applies efficient, random-field-like structured analysis, in a data-driven way, on the decoder outputs to enforce local label consensus. Although existing deep, saliency-based target detection networks for natural imagery rely on an analogous hierarchical processing pipeline for integrating local and global image cues, we consider a novel multi-branching structure. We also post-process the saliency estimates as part of the network without the need for recurrent layers. Doing so significantly reduces the number of tunable parameters. Such traits aid in isolating targets well.

Our experimental results with real-world CSAS imagery showcased the MB-CEDNs' capabilities. They indicated that MB-CEDNs outperform conventional deep-network architectures trained in a supervised manner. This was a byproduct of using an architecture that derived multi-scale contrast features, which were able to isolate differently sized targets well. It was also due to having fewer filter redundancies than other deep networks. The ability to detect targets well largely stemmed from the interaction of the supervised and unsupervised decoder branches, though. Each branch provided a unique interpretation of the underwater scenes which, when combined, offered a more accurate solution than either branch alone. Processing multiple CSAS images simultaneously also improved the detection rate when complete-aperture information for a target was lost.

Additionally, our MB-CEDNs greatly outperformed unsupervised, saliency-based approaches for target detection that are the state-of-the-art for object detection and segmentation in natural imagery. Such approaches make assumptions that, while applicable to natural imagery, do not extend to sonar imagery. Without either a fundamental shift in how they extract and utilize image cues or an ability to adapt those cues in a data-driven manner, they cannot hope to achieve the same detection and segmentation behaviors as deep networks for this modality.

Although our emphasis has been on target analysis for CSAS imagery, the network can, after re-training, also be applicable to SSAS imagery. In our future work, we will demonstrate that training on the sonar-image sub-apertures from the circular-scan case facilitates transfer learning to the side-scan case. Little to no re-training may therefore be necessary to achieve good detection and segmentation performance for SSAS, regardless of the target aspect angle. Moreover, such a transfer-learning process will significantly reduce the amount of human annotation efforts needed for supervised and semi-supervised training. Only the CSAS image, not each of the ensuing SSAS-derived images, needs to be annotated; any labels can be automatically propagated from the original CSAS image to the sub-apertures.

References

- [1] M. P. Hayes and P. T. Gough, "Synthetic aperture sonar: A review of current status," *IEEE Journal of Oceanic Engineering*, vol. 34, no. 3, pp. 207–224, 2009. Available: <http://dx.doi.org/10.1109/JOE.2009.2020853>
- [2] T. M. Marston, J. L. Kennedy, and P. L. Marston, "Coherent and semi-coherent processing of limited-aperture circular synthetic aperture (CSAS) data," in *Proceedings of the IEEE/MTS OCEANS Conference*, Waikoloa, HI, USA, September 19-22 2011, pp. 1–6. Available: <http://dx.doi.org/10.23919/OCEANS.2011.6107280>
- [3] T. Marston, "A correlation-based autofocus algorithm for coherent circular synthetic aperture sonar," in *Proceedings of the European Conference on Synthetic Aperture Radar (EUSAR)*, Nuremberg, Germany, April 23-26 2012, pp. 66–69.
- [4] T. M. Marston and J. L. Kennedy, "Volumetric acoustic imaging via circular multipass aperture synthesis," *IEEE Journal of Oceanic Engineering*, vol. 41, no. 4, pp. 852–867, 2016. Available: <http://dx.doi.org/10.1109/JOE.2015.2502664>
- [5] J. L. Kennedy, T. M. Marston, K. Lee, J. L. Lopes, and R. Lim, "A rail system for circular synthetic aperture sonar imaging and acoustic target strength measurements: Design/operation/preliminary results," *Review of Scientific Instruments*, vol. 85, no. 1, pp. 014901(1–10), 2014. Available: <http://dx.doi.org/10.1063/1.4861353>
- [6] S. K. Mitchell and S. P. Pitt, "SAS imaging of proud and buried targets at search frequencies," in *Proceedings of the IEEE/MTS OCEANS Conference*, Biloxi, MI, USA, October 29-31 2002, pp. 2279–2283. Available: <http://dx.doi.org/10.1109/OCEANS.2002.1191985>
- [7] B. G. Ferguson and R. J. Wyber, "Generalized framework for real aperture, synthetic aperture, and tomographic sonar imaging," *IEEE Journal of Oceanic Engineering*, vol. 34, no. 3, pp. 225–238, 2009. Available: <http://dx.doi.org/10.1109/JOE.2009.2017801>
- [8] M. Valdenegro-Toro, "Object recognition in forward-looking sonar images with convolutional neural networks," in *Proceedings of the IEEE/MTS OCEANS Conference*, Monterey, CA, USA, September 19-23 2016, pp. 1–6. Available: <http://dx.doi.org/10.1109/OCEANS.2016.7761140>

- [9] K. Denos, M. Ravaut, A. Fagette, and H.-K. Lim, "Deep learning applied to underwater mine warfare," in *Proceedings of the IEEE/MTS OCEANS Conference*, Aberdeen, UK, June 19-22 2017, pp. 1-7. Available: <http://dx.doi.org/10.1109/OCEANSE.2017.8084910>
- [10] L. Jin and H. Liang, "Deep learning for underwater image recognition in small sample size situations," in *Proceedings of the IEEE/MTS OCEANS Conference*, Aberdeen, UK, June 19-22 2017, pp. 1-4. Available: <http://dx.doi.org/10.1109/OCEANSE.2017.8084645>
- [11] D. Kohntopp, B. Lehmann, D. Kraus, and A. Birk, "Seafloor classification for mine countermeasures operations using synthetic aperture sonar images," in *Proceedings of the IEEE/MTS OCEANS Conference*, Aberdeen, UK, June 19-22 2017, pp. 1-5. Available: <http://dx.doi.org/10.1109/OCEANSE.2017.8084752>
- [12] D. P. Williams, "Exploiting phase information in synthetic aperture sonar images for target classification," in *Proceedings of the IEEE/MTS OCEANS Conference*, Kobe, Japan, May 28-31 2018, pp. 1-6. Available: <http://dx.doi.org/10.1109/OCEANSKOB.2018.8559255>
- [13] W. K. Stewart, M. Jiang, and M. Marra, "A neural network approach to classification of sidescan sonar imagery from a midocean ridge area," *IEEE Journal of Oceanic Engineering*, vol. 19, no. 2, pp. 214-224, 1994. Available: <http://dx.doi.org/10.1109/48.286644>
- [14] S. W. Perry and L. Guan, "A recurrent neural network for detecting objects in sequences of sector-scan sonar images," *IEEE Journal of Oceanic Engineering*, vol. 29, no. 3, pp. 857-871, 2004. Available: <http://dx.doi.org/10.1109/JOE.2004.831616>
- [15] Z.-H. Michalopoulou, D. Alexandrou, and C. de Moustier, "Application of neural and statistical classifiers to the problem of seafloor characterization," *IEEE Journal of Oceanic Engineering*, vol. 20, no. 3, pp. 190-197, 1995. Available: <http://dx.doi.org/10.1109/48.393074>
- [16] B. Chakraborty, V. Kodagali, and J. Baracho, "Sea-floor classification using multibeam echo-sounding angular backscatter data: A real-time approach employing hybrid neural network architecture," *IEEE Journal of Oceanic Engineering*, vol. 28, no. 1, pp. 121-128, 2003. Available: <http://dx.doi.org/10.1109/JOE.2002.808211>
- [17] D. P. Williams and S. Dugelay, "Multi-view SAS image classification using deep learning," in *Proceedings of the IEEE/MTS OCEANS Conference*, Monterey, CA, USA, September 19-23 2016, pp. 1-9. Available: <http://dx.doi.org/10.1109/OCEANS.2016.7761334>
- [18] M. I. Petterson, V. Zetterberg, and I. Claesson, "Detection and imaging of moving targets in wide band SAS using fast time backprojection combined with spate time processing," in *Proceedings of the IEEE/MTS OCEANS Conference*, Washington, DC, USA, September 17-23 2005, pp. 2388-2393. Available: <http://dx.doi.org/10.1109/OCEANS.2005.1640123>
- [19] E. Dura, Y. Zhang, X. Liao, G. J. Dobeck, and L. Carin, "Active learning for detection of mine-like objects in side-scan sonar imagery," *IEEE Journal of Oceanic Engineering*, vol. 30, no. 2, pp. 360-371, 2005. Available: <http://dx.doi.org/10.1109/JOE.2005.850931>
- [20] J. Cartmill, N. Wachowski, and M. R. Azimi-Sadjadi, "Buried underwater object classification using a collaborative multispect classifier," *IEEE Journal of Oceanic Engineering*, vol. 34, no. 1, pp. 32-44, 2009. Available: <http://dx.doi.org/10.1109/JOE.2008.2008041>
- [21] K. Mukherjee, S. Gupta, A. Ray, and S. Phoha, "Symbolic analysis of sonar data for underwater target detection," *IEEE Journal of Oceanic Engineering*, vol. 36, no. 2, pp. 219-230, 2011. Available: <http://dx.doi.org/10.1109/JOE.2011.2122590>
- [22] R. Fandos, A. M. Zoubir, and K. Siantidis, "Unified design of a feature-based ADAC system for mine hunting using synthetic aperture sonar," *IEEE Transactions on Geoscience and Remote Sensing*, vol. 52, no. 5, pp. 2413-2426, 2014. Available: <http://dx.doi.org/10.1109/TGRS.2013.2260863>
- [23] T. Fei, D. Kraus, and A. M. Zoubir, "Contributions to automatic target recognition systems for underwater mine classification," *IEEE Transactions on Geoscience and Remote Sensing*, vol. 53, no. 1, pp. 505-518, 2015. Available: <http://dx.doi.org/10.1109/TGRS.2014.2324971>
- [24] T. Berthomier, D. P. Williams, and S. Dugelay, "Target localization in synthetic aperture sonar imagery using convolutional neural networks," in *Proceedings of the IEEE/MTS OCEANS Conference*, Seattle, WA, USA, October 27-31 2019, pp. 1-9. Available: <http://dx.doi.org/10.23919/OCEANS40490.2019.8962774>
- [25] A. Abu and R. Diamant, "Unsupervised segmentation of underwater objects in sonar images," in *Proceedings of the IEEE/MTS OCEANS Conference*, Aberdeen, UK, June 19-22 2017, pp. 1-5. Available: <http://dx.doi.org/10.1109/OCEANSE.2017.8084853>
- [26] V. Chandran, S. Elgar, and A. Nguyen, "Detection of mines in acoustic images using higher order spectral features," *IEEE Journal of Oceanic Engineering*, vol. 27, no. 3, pp. 610-618, 2002. Available: <http://dx.doi.org/10.1109/JOE.2002.1040943>
- [27] A. Pezeshki, M. R. Azimi-Sadjadi, and L. L. Scharf, "Undersea target classification using canonical correlation analysis," *IEEE Journal of Oceanic Engineering*, vol. 32, no. 4, pp. 948-955, 2007. Available: <http://dx.doi.org/10.1109/JOE.2007.907926>
- [28] E. Dura, J. Bell, and D. Lane, "Superellipse fitting for the recovery and classification of mine-like shapes in sidescan sonar images," *IEEE Journal of Oceanic Engineering*, vol. 33, no. 4, pp. 434-444, 2008. Available: <http://dx.doi.org/10.1109/JOE.2008.2002962>
- [29] J. D. Tucker and M. R. Azimi-Sadjadi, "Coherence-based underwater target detection from multiple disparate sonar platforms," *IEEE Journal of Oceanic Engineering*, vol. 36, no. 1, pp. 37-51, 2011. Available: <http://dx.doi.org/10.1109/JOE.2010.2094230>
- [30] D. P. Williams, "Fast target detection in synthetic aperture sonar imagery: A new algorithm and large-scale performance analysis," *IEEE Journal of Oceanic Engineering*, vol. 40, no. 1, pp. 71-92, 2015. Available: <http://dx.doi.org/10.1109/JOE.2013.2294532>
- [31] R. Fandos and A. M. Zoubir, "Optimal feature set for automatic detection and classification of underwater objects in SAS images," *IEEE Journal of Selected Topics in Signal Processing*, vol. 5, no. 3, pp. 454-468, 2010.

Available: <http://dx.doi.org/10.1109/JSTSP.2010.2093868>

[32] A. Abu and R. Diamant, "Enhanced fuzzy-based local information algorithm for sonar image segmentation," *IEEE Transactions on Image Processing*, vol. 29, no. 1, pp. 445–460, 2019. Available: <http://dx.doi.org/10.1109/TIP.2019.2930148>

[33] P. Sermanet, D. Eigen, X. Zhang, M. Mathieu, F. Fergus, and Y. LeCun, "OverFeat: Integrated recognition, localization, and detection using convolutional networks," in *Proceedings of the International Conference on Learning Representations (ICLR)*, Banff, Canada, April 14-16 2014, pp. 1–15. Available: <https://arxiv.org/abs/1312.6229>

[34] R. Girshick, J. Donahue, T. Darrell, and J. Malik, "Rich feature hierarchies for accurate object detection and semantic segmentation," in *Proceedings of the IEEE International Conference on Computer Vision and Pattern Recognition (CVPR)*, Columbus, OH, USA, June 23-28 2014, pp. 580–587. Available: <http://dx.doi.org/10.1109/CVPR.2014.81>

[35] J. Redmon, S. Divvala, R. Girshick, and A. Farhadi, "You only look once: Unified, real-time object detection," in *Proceedings of the IEEE International Conference on Computer Vision and Pattern Recognition (CVPR)*, Las Vegas, NV, USA, June 27-30 2016, pp. 779–788. Available: <http://dx.doi.org/10.1109/CVPR.2016.91>

[36] J. Redmon and A. Farhadi, "YOLO9000: Better, faster, stronger," in *Proceedings of the IEEE International Conference on Computer Vision and Pattern Recognition (CVPR)*, Honolulu, HI, USA, July 21-26 2017, pp. 6517–6525. Available: <http://dx.doi.org/10.1109/CVPR.2017.690>

[37] D. G. Lowe, "Object recognition from local scale-invariant features," in *Proceedings of the IEEE International Conference on Computer Vision (ICCV)*, Kerkyra, Greece, September 20-27 1999, pp. 1150–1157. Available: <http://dx.doi.org/10.1109/ICCV.1999.790410>

[38] N. Dalal and B. Triggs, "Histograms of oriented gradients for human detection," in *Proceedings of the IEEE International Conference on Computer Vision and Pattern Recognition (CVPR)*, San Diego, CA, USA, June 20-25 2005, pp. 866–893. Available: <http://dx.doi.org/10.1109/CVPR.2005.177>

[39] K. E. A. van de Sande, J. R. R. Uiglings, T. Gevers, and A. W. M. Smeulders, "Segmentation as selective search for object recognition," in *Proceedings of the IEEE International Conference on Computer Vision (ICCV)*, Barcelona, Spain, November 6-13 2014, pp. 1879–1886. Available: <http://dx.doi.org/10.1109/ICCV.2014.6126456>

[40] K. He, X. Zhang, S. Ren, and J. Sun, "Spatial pyramid pooling in deep convolutional networks for visual recognition," in *Proceedings of the European Conference on Computer Vision (ECCV)*, Zurich, Switzerland, September 6-12 2014, pp. 346–361. Available: <http://dx.doi.org/10.1007/978-3-319-10578-9>

[41] R. Girshick, "Fast R-CNN," in *Proceedings of the IEEE International Conference on Computer Vision (ICCV)*, Santiago, Chile, December 7-13 2015, pp. 1440–1448. Available: <http://dx.doi.org/10.1109/ICCV.2015.169>

[42] S. Ren, K. He, R. Girshick, and J. Sun, "Faster R-CNN: Towards real-time object detection with region proposal frameworks," in *Advances in Neural Information Processing Systems (NIPS)*, C. Cortes, N. D. Lawrence, D. D. Lee, M. Sugiyama, and R. Garnett, Eds. Red Hook, NY, USA: Curran Associates, 2015, pp. 91–99.

[43] J. Dai, Y. Li, K. He, and J. Sun, "R-FCN: Object detection via region-based fully convolutional networks," in *Advances in Neural Information Processing Systems (NIPS)*, D. D. Lee, M. Sugiyama, U. V. Luxburg, I. Guyon, and R. Garnett, Eds. Red Hook, NY, USA: Curran Associates, 2016, pp. 379–387.

[44] J. Long, E. Shelhamer, and T. Darrell, "Fully convolutional networks for semantic segmentation," in *Proceedings of the IEEE International Conference on Computer Vision and Pattern Recognition (CVPR)*, Boston, MA, USA, June 7-12 2015, pp. 3431–3440. Available: <http://dx.doi.org/10.1109/CVPR.2015.7298965>

[45] B. Hariharan, P. Arbeláez, R. Girshick, and J. Malik, "Hypercolumns for object segmentation and fine-grained localization," in *Proceedings of the IEEE International Conference on Computer Vision and Pattern Recognition (CVPR)*, Boston, MA, USA, June 7-12 2015, pp. 447–456. Available: <http://dx.doi.org/10.1109/CVPR.2015.7298642>

[46] T. Kong, A. Yao, Y. Chen, and F. Sun, "HyperNet: Towards accurate region proposal generation and joint object detection," in *Proceedings of the IEEE International Conference on Computer Vision and Pattern Recognition (CVPR)*, Las Vegas, NV, USA, June 27-30 2016, pp. 845–853. Available: <http://dx.doi.org/10.1109/CVPR.2016.98>

[47] S. Bell, C. L. Zitnick, K. Bala, and R. Girshick, "Inside-outside net: Detecting objects in context with skip pooling and recurrent neural networks," in *Proceedings of the IEEE International Conference on Computer Vision and Pattern Recognition (CVPR)*, Las Vegas, NV, USA, June 27-30 2016, pp. 2874–2883. Available: <http://dx.doi.org/10.1109/CVPR.2016.314>

[48] W. Liu, A. Rabinovich, and A. C. Berg, "ParseNet: Looking wider to see better," in *Proceedings of the International Conference on Learning Representations (ICLR)*, San Juan, Puerto Rico, May 2-4 2016, pp. 1–11. Available: <https://arxiv.org/abs/1506.04579>

[49] W. Liu, D. Anguelov, D. Erhan, C. Szegedy, S. Reed, C.-Y. Fu, and A. C. Berg, "SSD: Single shot multibox detector," in *Proceedings of the European Conference on Computer Vision (ECCV)*, Amsterdam, Netherlands, October 8-16 2016, pp. 21–37. Available: <http://dx.doi.org/10.1007/978-3-319-46448-0>

[50] Z. Cai, Q. Fan, R. S. Feris, and N. Vasconcelos, "A unified multi-scale deep convolutional neural network for fast object detection," in *Proceedings of the European Conference on Computer Vision (ECCV)*, Amsterdam, Netherlands, October 8-16 2016, pp. 354–370. Available: <http://dx.doi.org/10.1007/978-3-319-46493-0>

[51] S. Kohl, et al., "A probabilistic UNet for segmentation of ambiguous images," in *Advances in Neural Information Processing Systems (NIPS)*, S. Bengio, H. Wallach, H. Larochelle, K. Grauman, N. Cesa-Bianchi, and R. Garnett, Eds. Red Hook, NY, USA: Curran Associates, 2018, pp. 6965–6975.

[52] P. O. Pinheiro, R. Collobert, and P. Dollár, "Learning to segment object candidates," in *Advances in Neural Information Processing Systems (NIPS)*, C. Cortes, N. D. Lawrence, D. D. Lee, M. Sugiyama, and R. Garnett, Eds. Red Hook, NY, USA: Curran Associates, 2015, pp. 1990–1998.

- [53] P. O. Pinheiro, T.-Y. Lin, R. Collobert, and P. Dollár, "Learning to refine object segments," in *Proceedings of the European Conference on Computer Vision (ECCV)*, Amsterdam, Netherlands, October 8-16 2016, pp. 75–91. Available: <http://dx.doi.org/10.1007/978-3-319-46493-0>
- [54] G. Ghiasi and C. C. Fowlkes, "Laplacian pyramid reconstruction and refinement for semantic segmentation," in *Proceedings of the European Conference on Computer Vision (ECCV)*, Amsterdam, Netherlands, October 8-16 2016, pp. 519–534. Available: <http://dx.doi.org/10.1007/978-3-319-46493-0>
- [55] S. Yu and J. C. Príncipe, "Understanding autoencoders with information-theoretic concepts," *Neural Networks*, vol. 117, no. 1, pp. 104–123, 2019. Available: <http://dx.doi.org/10.1016/j.neunet.2019.05.003>
- [56] S. Yu, K. Wickstrøm, R. Jenssen, and J. C. Príncipe, "Understanding convolutional neural network training with information theory," *IEEE Transactions on Information Theory*, 2018, (under review). Available: <https://arxiv.org/abs/1804.06537>
- [57] G. Papandreou, L.-C. Chen, K. P. Murphy, and A. L. Yuille, "Weakly and semi-supervised learning of a deep convolutional network for semantic image segmentation," in *Proceedings of the IEEE International Conference on Computer Vision (ICCV)*, Santiago, Chile, December 7-13 2015, pp. 1742–1750. Available: <http://dx.doi.org/10.1109/ICCV.2015.203>
- [58] N. Souly, C. Spampinato, and M. Shah, "Semi supervised semantic segmentation using generative adversarial networks," in *Proceedings of the IEEE International Conference on Computer Vision (ICCV)*, Venice, Italy, December 7-13 2017, pp. 5689–5697. Available: <http://dx.doi.org/10.1109/ICCV.2017.606>
- [59] Y. Wei, J. Feng, X. Liang, M.-M. Cheng, Y. Zhao, and S. Yan, "Object region mining with adversarial erasing: A simple classification to semantic segmentation approach," in *Proceedings of the IEEE International Conference on Computer Vision and Pattern Recognition (CVPR)*, Honolulu, HI, USA, July 21-26 2017, pp. 6488–6496. Available: <http://dx.doi.org/10.1109/CVPR.2017.687>
- [60] Y. Wei, H. Xiao, H. Shi, Z. Jie, J. Feng, and T. S. Huang, "Revisiting dilated convolution: A simple approach for weakly- and semi-supervised semantic segmentation," in *Proceedings of the IEEE International Conference on Computer Vision and Pattern Recognition (CVPR)*, Salt Lake City, UT, USA, June 18-23 2018, pp. 7268–7277. Available: <http://dx.doi.org/10.1109/CVPR.2018.00759>
- [61] H. Noh, S. Hong, and B. Han, "Learning deconvolution network for semantic segmentation," in *Proceedings of the IEEE International Conference on Computer Vision (ICCV)*, Santiago, Chile, December 7-13 2015, pp. 1520–1528. Available: <http://dx.doi.org/10.1109/ICCV.2015.178>
- [62] D. Parkhurst, K. Law, and E. Niebur, "Modeling the role of salience in the allocation of overt visual attention," *Vision Research*, vol. 42, no. 2, pp. 107–123, 2002. Available: [http://dx.doi.org/10.1016/s0042-6989\(01\)00250-4](http://dx.doi.org/10.1016/s0042-6989(01)00250-4)
- [63] W. Einhäuser and P. König, "Does luminance-contrast contribute to a saliency map for overt visual attention?" *European Journal of Neuroscience*, vol. 17, no. 5, pp. 1089–1097, 2003. Available: <http://dx.doi.org/10.1046/j.1460-9568.2003.02508.x>
- [64] V. Nair and G. E. Hinton, "Rectified linear units improve restricted Boltzmann machines," in *Proceedings of the International Conference on Machine Learning (ICML)*, Haifa, Israel, June 21-24 2010, pp. 807–814.
- [65] L.-C. Chen, G. Papandreou, I. Kokkinos, K. Murphy, and A. L. Yuille, "Deeplab: Semantic image segmentation with deep convolutional nets, atrous convolution, and fully connected CRFs," *IEEE Transactions on Pattern Analysis and Machine Intelligence*, vol. 40, no. 4, pp. 834–848, 2018. Available: <http://dx.doi.org/10.1109/TPAMI.2017.2699184>
- [66] M. Oquab, L. Bottou, I. Laptev, and J. Sivic, "Is object localization for free? Weakly-supervised learning with convolutional neural networks," in *Proceedings of the IEEE International Conference on Computer Vision and Pattern Recognition (CVPR)*, Boston, MA, USA, June 7-12 2015, pp. 685–694. Available: <http://dx.doi.org/10.1109/CVPR.2015.7298668>
- [67] B. Zhou, A. Khosla, A. Lapedriza, A. Oliva, and A. Torralba, "Learning deep features for discriminative localization," in *Proceedings of the IEEE International Conference on Computer Vision and Pattern Recognition (CVPR)*, Las Vegas, NV, USA, June 27-30 2016, pp. 2921–2929. Available: <http://dx.doi.org/10.1109/CVPR.2016.319>
- [68] M. Liang and X. Hu, "Recurrent convolutional neural network for object recognition," in *Proceedings of the IEEE International Conference on Computer Vision and Pattern Recognition (CVPR)*, Boston, MA, USA, June 7-12 2015, pp. 3367–3375. Available: <http://dx.doi.org/10.1109/CVPR.2015.7298958>
- [69] N. Liu and J. Han, "DHSNet: Deep hierarchical saliency network for salient object detection," in *Proceedings of the IEEE International Conference on Computer Vision and Pattern Recognition (CVPR)*, Las Vegas, NV, USA, June 27-30 2016, pp. 678–686. Available: <http://dx.doi.org/10.1109/CVPR.2016.80>
- [70] R. K. Srivastava, K. Greff, and J. Schmidhuber, "Training very deep networks," in *Advances in Neural Information Processing Systems (NIPS)*, C. Cortes, N. D. Lawrence, D. D. Lee, M. Sugiyama, and R. Garnett, Eds. Cambridge, MA, USA: MIT Press, 2015, pp. 2377–2385.
- [71] A. E. Orhan and X. Pitkow, "Skip connections eliminate singularities," in *Proceedings of the International Conference on Learning Representations (ICLR)*, Vancouver, Canada, April 30-May 3 2018, pp. 1–22. Available: <https://arxiv.org/abs/1701.09175>
- [72] G. Huang, Z. Liu, L. van der Maaten, and K. Q. Weinberger, "Densely connected convolutional networks," in *Proceedings of the IEEE International Conference on Computer Vision and Pattern Recognition (CVPR)*, Honolulu, HI, USA, July 21-26 2017, pp. 2261–2269. Available: <http://dx.doi.org/10.1109/CVPR.2017.243>
- [73] S. Ioffe and C. Szegedy, "Batch normalization: Accelerating deep network training by reducing internal covariate shift," in *Proceedings of the International Conference on Machine Learning (ICML)*, Lille, France, July 6-11 2015, pp. 448–456.
- [74] S. Santurkar, D. Tsipras, A. Ilyas, and A. Madry, "How does batch normalization help optimization?" in *Advances in Neural Information Processing Systems (NIPS)*, S. Bengio, H. Wallach, H. Larochelle, K. Grauman, N. Cesa-Bianchi, and R. Garnett, Eds. Red Hook, NY, USA: Curran Associates, 2018, pp. 2483–2493.

- [75] A. Dosovitskiy, P. Fischer, E. Ilg, P. Häusser, C. Hazirbas, V. Golkov, P. van der Smagt, D. Cremers, and T. Brox, "FlowNet: Learning optical flow with convolutional networks," in *Proceedings of the IEEE International Conference on Computer Vision (ICCV)*, Santiago, Chile, December 7-13 2015, pp. 2758–2766. Available: <http://dx.doi.org/10.1109/ICCV.2015.316>
- [76] E. Ilg, N. Mayer, T. Saikia, M. Keuper, A. Dosovitskiy, and T. Brox, "FlowNet 2.0: Evolution of optical flow estimation with deep networks," in *Proceedings of the IEEE International Conference on Computer Vision and Pattern Recognition (CVPR)*, Honolulu, HI, USA, July 21-26 2017, pp. 1647–1655. Available: <http://dx.doi.org/10.1109/CVPR.2017.179>
- [77] T. W. Hui, X. Tang, and C. C. Loy, "LiteFlowNet: A lightweight convolutional neural network for optical flow estimation," in *Proceedings of the IEEE International Conference on Computer Vision and Pattern Recognition (CVPR)*, Salt Lake City, UT, USA, June 18-23 2018, pp. 8981–8989. Available: <http://dx.doi.org/10.1109/CVPR.2018.00936>
- [78] S. R. Buló, P. Kotschieder, M. Pelillo, and H. Bischof, "Structured local predictors for image labeling," in *Proceedings of the IEEE International Conference on Computer Vision and Pattern Recognition (CVPR)*, Providence, RI, USA, June 16-21 2012, pp. 3530–3537. Available: <http://dx.doi.org/10.1109/CVPR.2012.6248096>
- [79] Z. Liu, X. Li, P. Luo, C. C. Loy, and X. Tang, "Deep learning Markov random field for semantic segmentation," *IEEE Transactions on Pattern Analysis and Machine Intelligence*, vol. 40, no. 8, pp. 1814–1828, 2017. Available: <http://dx.doi.org/10.1109/TPAMI.2017.2737535>
- [80] Q. Hou, M.-M. Cheng, X. Hu, A. Borji, Z. Tu, and P. H. S. Torr, "Deeply supervised salient object detection with short connections," in *Proceedings of the IEEE International Conference on Computer Vision and Pattern Recognition (CVPR)*, Honolulu, HI, USA, July 21-26 2017, pp. 5300–5309. Available: <http://dx.doi.org/10.1109/CVPR.2017.563>
- [81] Z. Lou, A. Mishra, A. Ackhar, J. Eichel, S. Li, and P.-M. Jodoin, "Non-local deep features for salient object detection," in *Proceedings of the IEEE International Conference on Computer Vision and Pattern Recognition (CVPR)*, Honolulu, HI, USA, July 21-26 2017, pp. 6593–6601. Available: <http://dx.doi.org/10.1109/CVPR.2017.698>
- [82] P. Zhang, D. Wang, H. Lu, H. Wang, and B. Yin, "Learning uncertain convolutional features for accurate saliency detection," in *Proceedings of the IEEE International Conference on Computer Vision (ICCV)*, Venice, Italy, December 7-13 2017, pp. 212–221. Available: <http://dx.doi.org/10.1109/ICCV.2017.32>
- [83] T. Wang, A. Borji, L. Zhang, P. Zhang, and H. Lu, "A stagewise refinement model for detecting salient objects in images," in *Proceedings of the IEEE International Conference on Computer Vision (ICCV)*, Venice, Italy, December 7-13 2017, pp. 4039–4048. Available: <http://dx.doi.org/10.1109/ICCV.2017.433>
- [84] X. Li, L. Zhao, L. Wei, M.-H. Yang, F. Wu, Y. Zhuang, H. Ling, and J. Wang, "DeepSaliency: Multi-task deep neural network model for salient object detection," *IEEE Transactions on Image Processing*, vol. 25, no. 8, pp. 3919–3930, 2016. Available: <http://dx.doi.org/10.1109/TIP.2016.2579306>
- [85] L. Wang, L. Wang, H. Lu, P. Zhang, and X. Ruan, "Salient object detection with recurrent fully convolutional networks," *IEEE Transactions on Pattern Analysis and Machine Intelligence*, vol. 41, no. 7, pp. 1734–1746, 2019. Available: <http://dx.doi.org/10.1109/TPAMI.2018.2846598>
- [86] L. Itti, C. Koch, and W. Niebur, "A model of saliency-based visual attention for rapid scene analysis," *IEEE Transactions on Pattern Analysis and Machine Intelligence*, vol. 20, no. 11, pp. 1254–1259, 1998. Available: <http://dx.doi.org/10.1109/34.730558>
- [87] Z. Zhang and M. Sabuncu, "Generalized cross entropy loss for training deep neural networks with noisy labels," in *Advances in Neural Information Processing Systems (NIPS)*, S. Bengio, H. Wallach, H. Larochelle, K. Grauman, N. Cesa-Bianchi, and R. Garnett, Eds. Red Hook, NY, USA: Curran Associates, 2018, pp. 8778–8788.
- [88] D. Zhang, J. Han, and Y. Zhang, "Supervision by fusion: Towards unsupervised learning of deep salient object detectors," in *Proceedings of the IEEE International Conference on Computer Vision (ICCV)*, Venice, Italy, October 22-29 2017, pp. 4068–4076. Available: <http://dx.doi.org/10.1109/ICCV.2017.436>
- [89] J. Whitehill, T.-F. Wu, J. Bergsma, J. R. Movellan, and P. L. Ruvolo, "Whose vote should count more: Optimal integration of labels from labelers of unknown expertise," in *Advances in Neural Information Processing Systems (NIPS)*, Y. Bengio, D. Schuurmans, J. D. Lafferty, C. K. I. Williams, and A. Culotta, Eds. Red Hook, NY, USA: Curran Associates, 2009, pp. 2035–2043.
- [90] M. P. Kumar, B. Packer, and D. Koller, "Self-paced learning for latent variable models," in *Advances in Neural Information Processing Systems (NIPS) Workshop*, H. Lee, M. Ranzato, Y. Bengio, G. E. Hinton, Y. LeCun, and A. Y. Ng, Eds. Cambridge, MA, USA: MIT Press, 2010, pp. 1189–1197.
- [91] Y. Bengio, J. Louradour, R. Collobert, and J. Weston, "Curriculum learning," in *Proceedings of the International Conference on Machine Learning (ICML)*, Montreal, Canada, June 14-18 2009, pp. 41–48. Available: <http://dx.doi.org/10.1145/1553374.1553380>
- [92] W. I. Zangwill, *Nonlinear Programming: A Unified Approach*. Upper Saddle River, NJ, USA: Prentice-Hall, 1969.
- [93] D. P. Kingma and J. Ba, "ADAM: A method for stochastic optimization," in *Proceedings of the International Conference on Learning Representations (ICLR)*, San Diego, CA, USA, May 7-9 2015, pp. 1–15. Available: <https://arxiv.org/abs/1412.6980>
- [94] M. Hardt, B. Recht, and Y. Singer, "Train faster, generalize better: Stability of stochastic gradient descent," in *Proceedings of the International Conference on Machine Learning (ICML)*, New York, NY, USA, June 19-24 2016, pp. 1225–1234.
- [95] R. Achanta, S. Hemami, F. Estrada, and S. Sussstrunk, "Frequency-tuned salient region detection," in *Proceedings of the IEEE International Conference on Computer Vision and Pattern Recognition (CVPR)*,

Miami, FL, USA, June 20-25 2009, pp. 1597–1604. Available: <http://dx.doi.org/10.1109/CVPR.2009.5206596>

[96] R. Zhao, W. Quyang, H. Li, and X. Wang, “Saliency detection by multi-context deep learning,” in *Proceedings of the IEEE International Conference on Computer Vision and Pattern Recognition (CVPR)*, Boston, MA, USA, June 7-12 2015, pp. 1265–1274. Available: <http://dx.doi.org/10.1109/CVPR.2015.7298731>

[97] W. Zhu, S. Liang, Y. Wei, and J. Sun, “Saliency optimization from robust background detection,” in *Proceedings of the IEEE International Conference on Computer Vision and Pattern Recognition (CVPR)*, Columbus, OH, USA, June 23-23 2014, pp. 2814–2821. Available: <http://dx.doi.org/10.1109/CVPR.2014.360>

[98] F. Perazzi, P. Krähenbühl, Y. Pritch, and A. Hornung, “Saliency filters: Contrast-based filtering for salient region detection,” in *Proceedings of the IEEE International Conference on Computer Vision and Pattern Recognition (CVPR)*, Providence, RI, USA, June 16-21 2012, pp. 733–740. Available: <http://dx.doi.org/10.1109/CVPR.2012.6247743>

[99] Y. Zeng, H. Lu, L. Zhang, M. Feng, and A. Borji, “Learning to promote saliency detectors,” in *Proceedings of the IEEE International Conference on Computer Vision and Pattern Recognition (CVPR)*, Salt Lake City, UT, USA, June 18-23 2018, pp. 1644–1653. Available: <http://dx.doi.org/10.1109/CVPR.2018.00177>

[100] C. Yang, L. Zhang, H. Lu, X. Ruan, and M.-H. Yang, “Geodesic saliency using background priors,” in *Proceedings of the European Conference on Computer Vision (ECCV)*, Firenze, Italy, October 7-13 2012, pp. 29–42. Available: <http://dx.doi.org/10.1007/978-3-642-33712-30>

[101] J. Yang and M.-H. Yang, “Top-down visual saliency via joint CRF and dictionary learning,” in *Proceedings of the IEEE International Conference on Computer Vision and Pattern Recognition (CVPR)*, Providence, RI, USA, June 16-21 2012, pp. 2296–2303. Available: <http://dx.doi.org/10.1109/CVPR.2012.6247940>

[102] W.-C. Tu, S. He, Q. Yang, and S.-Y. Chien, “Real-time salient object detection with a minimum spanning tree,” in *Proceedings of the IEEE International Conference on Computer Vision and Pattern Recognition (CVPR)*, Las Vegas, NV, USA, June 27-30 2016, pp. 2334–2342. Available: <http://dx.doi.org/10.1109/CVPR.2016.256>

[103] Y. Qin, H. Lu, Y. Xu, and H. Wang, “Saliency detection via cellular automata,” in *Proceedings of the IEEE International Conference on Computer Vision and Pattern Recognition (CVPR)*, Boston, MA, USA, June 7-12 2015, pp. 110–119. Available: <http://dx.doi.org/10.1109/CVPR.2015.7298606>

[104] Q. Yan, L. Xu, J. Shi, and J. Jia, “Hierarchical saliency detection,” in *Proceedings of the IEEE International Conference on Computer Vision and Pattern Recognition (CVPR)*, Portland, OR, USA, June 23-28 2013, pp. 1155–1162. Available: <http://dx.doi.org/10.1109/CVPR.2013.153>

[105] C. Yang, L. Zhang, H. Lu, X. Ruan, and M.-H. Yang, “Saliency detection via graph-based manifold ranking,” in *Proceedings of the IEEE International Conference on Computer Vision and Pattern Recognition (CVPR)*, Portland, OR, USA, June 23-28 2013, pp. 3166–3173. Available: <http://dx.doi.org/10.1109/CVPR.2013.407>